

Impacts of atmospheric circulation patterns and cloud inhibition on aerosol radiative effect and boundary layer structure during winter air pollution in Sichuan Basin, China

Hua Lu^{1,3}, Min Xie^{2,6}, Bingliang Zhuang¹, Bojun Liu⁴, Yangzhihao Zhan¹, Tijian Wang¹, Shu Li¹, Mengmeng Li¹, Kuanguang Zhu^{1,5}

¹School of Atmospheric Sciences, Nanjing University, Nanjing 210023, China

²School of Environment, Nanjing Normal University, Nanjing 210023, China

³Chongqing Institute of Meteorological Sciences, Chongqing 401147, China

⁴Chongqing Meteorological Observatory, Chongqing 401147, China

⁵Hubei Provincial Academy of Eco-environmental Sciences, Wuhan 430079, China

⁶Carbon monitoring and digital application technology center, Carbon peak and carbon neutralization strategy institute of Jiangsu Province, Nanjing 210023, China

1 **Impacts of atmospheric circulation patterns and cloud** 2 **inhibition on aerosol radiative effect and boundary layer** 3 **structure during winter air pollution in Sichuan Basin,** 4 **China**

5 Hua Lu^{1,3}, Min Xie^{2,6}, Bingliang Zhuang¹, Bojun Liu⁴, Yangzhihao Zhan¹, Tijian
6 Wang¹, Shu Li¹, Mengmeng Li¹, Kuanguang Zhu^{1,5}

7
8 ¹School of Atmospheric Sciences, Nanjing University, Nanjing 210023, China

9 ²School of Environment, Nanjing Normal University, Nanjing 210023, China

10 ³Chongqing Institute of Meteorological Sciences, Chongqing 401147, China

11 ⁴Chongqing Meteorological Observatory, Chongqing 401147, China

12 ⁵Hubei Provincial Academy of Eco-environmental Sciences, Wuhan 430079, China

13 ⁶Carbon monitoring and digital application technology center, Carbon peak and carbon neutralization
14 strategy institute of Jiangsu Province, Nanjing 210023, China

15 *Correspondence to:* Min Xie (minxie@njnu.edu.cn)

16 **Abstract.** Winter persistent aerosol pollution frequently occurs in the Sichuan Basin (SCB) due to its
17 unfavorable weather conditions, such as low wind, wetness, and cloudiness. Based on long-term
18 observational data analyses from 2015–2021, it has been found that the four representative stations in
19 the SCB often simultaneously experience PM_{2.5} pollution accompanied by variations in meteorological
20 conditions above 850 hPa, which indicates a connection between regional winter air pollution in the
21 SCB and large-scale synoptic patterns. The dominant 850 hPa synoptic patterns of winter SCB were
22 classified into six patterns using T-model principal component analysis: (1) strong high pressure in the
23 north, (2) east high west low (EHWL) pressure, (3) weak high pressure in the north, (4) weak ridge of
24 high pressure after the trough, (5) low trough (LT), and (6) strong high pressure. Pattern 2
25 characterized with EHWL pressure system, and Pattern 5 featured with LT, were identified as key
26 synoptic patterns for the beginning and accumulation of pollution processes. Pattern 1, characterized by
27 a strong high pressure in the north, was the cleanest pattern associated with reduced PM_{2.5}
28 concentrations. The EHWL and LT patterns were associated with a remarkably high cloud liquid
29 content, attributed to upper southerly winds introducing humid air. Clouds reduce solar radiation
30 through reflection and scattering, resulting in more stable stratification and aerosol accumulation. This
31 cloud radiation interaction (CRI) was more pronounced in the LT pattern due to denser isobaric lines
32 and stronger southerly winds than in the EHWL pattern. Numerical simulation experiments utilizing
33 WRF-Chem indicated that there is an upper-level heating during afternoon and surface cooling in the
34 morning forced by the aerosol radiation interaction (ARI) under the EHWL and LT patterns.
35 Additionally, strong surface cooling in the evening influenced by valley winds could be found. With
36 wet and cloudy synoptic forcing, ARI directly affects the stability of the boundary layer and is
37 modulated through CRI inhibition. For example, Chongqing exhibited lower PM_{2.5} concentrations and
38 stronger ARI compared to the western and southern SCB due to lower cloud liquid content and weaker
39 CRI inhibition on ARI. The CRI inhibition caused a 50 % reduction in solar radiation and boundary

40 layer height during the daytime under the LT pattern, which was larger than that under the EHWL
41 pattern. This study comprehensively analyzed the spatial disparities in cloud inhibition on ARIs, their
42 impacts on the boundary layer structure, and the discrepancies of these interactions under different
43 synoptic patterns during pollution processes. The findings hold important implications for effective
44 management of pollution processes in cloudy and foggy weather.

45 Key words: Synoptic patterns, Cloud radiation interaction inhibition, Aerosol radiation interaction,
46 Boundary layer structure, Sichuan Basin.

47 **1 Introduction**

48 Particulate matter (PM) pollution has become a significant environmental concern in China (Xie
49 et al., 2016a; 2016b; Che et al., 2019). High concentrations of aerosols not only worsen air quality
50 and pose serious health risks to residents, but also have implications for weather and climate
51 through their effects on radiation and clouds (Li et al., 2019; Zhao et al., 2020; Alexeeff et al.,
52 2021; Yang et al., 2021). The interactions between aerosols and clouds present the largest
53 uncertainty in anthropogenic radiative forcing of the Earth's climate (Liao et al., 2017; Haywood
54 et al., 2021). Studying interactions among cloud, aerosol and radiation from an air quality perspective
55 is crucial for a scientific understanding of relationship between weather and pollution.

56 Excessive emissions are the essential cause of air pollution, with primary aerosol and secondary
57 aerosol formation playing significant roles in comprehending the complete picture of air pollution
58 (Peng et al., 2021). Besides, meteorological conditions not only influence on the formation of
59 secondary aerosols, but also govern the transportation and distribution of both primary and
60 secondary aerosols, and thereby impact regional and long-range air pollution (Zhu et al., 2018;
61 Luo et al., 2018; Nichol et al., 2020; Zhang et al., 2020; Jiang et al., 2021). PM and gaseous
62 pollutants, primarily transported by the planetary boundary layer (PBL), are directly or indirectly
63 influenced by various meteorological factors such as wind, relative humidity, PBL height (PBLH),
64 and solar radiation. These factors contribute to the multi-temporal and spatial distribution
65 characteristics through vertical and horizontal diffusion, physicochemical reactions, and dry and
66 wet deposition (Park et al., 2017; Shu et al., 2017; Zhan et al., 2019; Huang et al., 2019). Large-
67 scale synoptic forcing is considered the primary driving condition for meteorological factors, PBL
68 structure, and the resulting distribution of atmospheric pollutants (Miao et al., 2019; Ning et al.,
69 2019; Jiang et al., 2020; Li et al., 2021). Specific synoptic patterns can induce advection, which
70 largely determines the local PBL structure and development. PBL, located at the bottom of the
71 atmosphere, is responsible for the main exchange of heat, moisture, and matter between the surface
72 and the free troposphere (Stull, 1988). The fate of pollutants emitted near the surface, a significant
73 source of aerosols in the air, is largely controlled by the PBL (Garratt, 1994). The PBLH is often
74 used as a metric to characterize the capacity and dilution of pollutants (Seidel et al., 2010).
75 Synoptic patterns can directly determine the meteorological conditions of emitted pollutants and

76 influence their transport by regulating PBL thermal stratification and mechanical turbulence (Stull,
77 1988; Ning et al., 2018; Zhan et al., 2019; Jiang et al., 2021; Zhang et al., 2022).

78 Unfavorable meteorological conditions play a significant role in contributing to aerosol pollution.
79 When pollutants accumulate to a certain degree, aerosols can reduce surface solar radiation
80 through backscattering or absorbing solar radiation, leading to surface cooling. This decrease in
81 solar radiation and temperature near the ground weakens turbulent diffusion, suppresses the
82 convective development of the PBL, and lowers PBLH, which in turn exacerbates aerosol pollution
83 (Ding et al., 2016; Wang et al., 2018). Moreover, the increase in humidity caused by the decreased
84 surface saturation vapor pressure and inhibited water vapor diffusion enhances aerosol
85 hygroscopic growth accelerates liquid-phase and heterogeneous reactions, and contributes to
86 aerosol pollution (Pilinis et al., 1989). The positive feedback between unfavorable PBL
87 meteorology and increasing aerosols was found to be responsible for the majority of the increase
88 in PM_{2.5} during cumulative stages in various regions of eastern China affected by aerosol pollution,
89 including the North China Plain, the Guanzhong Plain, the Yangtze River Delta, the Two Lakes
90 Basin, the Pearl River Delta and the Northeast China Plain. But in the Sichuan Basin (SCB), the
91 feedback is weak due to the suppression of the cloudy mid-upper layer (Zhong et al., 2018; Zhong
92 et al., 2019). As for the aerosol-cloud interactions, arise from increasing aerosols acting as cloud
93 condensation nuclei in cloud and translating into larger concentrations of smaller cloud droplets,
94 leading to an increased cloud albedo reflecting more radiation back to space (Twomey, 1977;
95 Lohmann and Feichter, 2005). Even a marginal increase in cloud droplets above pristine conditions
96 in deep convective clouds causes more droplets to reach supercooled levels, which enhances latent
97 heat release and invigorates convection (Rosenfeld et al., 2009; Possner et al., 2015). Further
98 increases in cloud droplets result in direct radiative effects, reducing downward solar radiation,
99 cooling the surface, and inhibiting convection (Scott et al., 2016).

100 The SCB is surrounded by high mountains with cloudy and wet weather conditions. The mean
101 annual relative humidity in the SCB is around 75%, with cloud fraction exceeding 80%, and an
102 average of 1200 hours of sunshine per year. The Chengdu–Chongqing city cluster in the SCB
103 serves as the economic center of the upper reaches of the Yangtze River in China, accounting for
104 approximately 10 % of the country’s population. However, rapid industrialization and urbanization
105 in this region have resulted in severe air pollution. The SCB is recognized as one of the most
106 polluted regions in China, with high black carbon concentrations (Li et al., 2016; Cao et al., 2021).
107 The Qinghai–Tibet Plateau on the western edge of the SCB significantly influences the transport
108 and accumulation of pollutants through thermal and dynamic effects (Ning et al., 2017; Shu et al.,
109 2021). In addition, the Qinghai–Tibet topography leads to higher cloud water content over the SCB
110 than the other regions (Yu et al., 2004; Yang et al., 2012). Many studies have emphasized the
111 importance of the interactions between cloud, aerosols and radiation in air pollution processes (Wang et
112 al., 2018; Hu et al., 2021). High pollutant emissions, combined with the prevalence of cloudy and
113 foggy weather, make these interactions in the SCB even more complex than those in other regions. The
114 aerosol radiation interactions (ARI) can be inhibited by cloud in cities like Chengdu (Zhong et al.,

115 2019). However, there is a lack of in-depth quantitative discussions regarding this aspects in the SCB.
116 On one hand, the complex terrain in the SCB leads to differences in the meteorological conditions
117 between them (Ning et al., 2017; Lu et al., 2022). For example, Chengdu is a typical basin city while
118 Chongqing is a mountain city located on the basin slope, so they have markedly different climate
119 conditions. It remains to be elucidated whether these conditions will result in spatial disparities in cloud
120 inhibition on the ARI. On the other hand, synoptic forcing, as the primary driver of meteorological
121 variations, undoubtedly play an unneglectable role in shaping cloud cover and boundary layer
122 structures (Miao et al., 2020; Wang et al., 2022; Painemal et al., 2023). The discrepancies in cloud
123 inhibition on ARI under different synoptic patterns also need to be revealed. Addressing these issues is
124 crucial for understanding the persistent pollution processes and the intricate interactions between
125 weather and pollution in the SCB. It holds important implications for the effective management of
126 pollution processes in cloudy and foggy weather.

127 Characterized with high aerosol loadings and semi-permanent cloudy weather, the SCB
128 provides an ideal region for studying the complex interactions between clouds, aerosols, and the
129 PBL. This study objectively classifies the synoptic patterns influencing the SCB based on long-
130 term data. By conducting an integrated analysis of pollutants and meteorological factors, the
131 primary pollution sources and clean synoptic patterns are identified. To further investigate the
132 inhibition of cloud radiation interaction (CRI) on ARI under different synoptic patterns in the SCB,
133 WRF-CHEM simulation experiments are conducted. The results contribute to a deeper
134 understanding of CRI, ARI, and the PBL interactions in regions influenced by plateau-basin
135 topography with wet and cloudy weather. The data and methods are presented in Section 2,
136 whereas Section 3 describes the synoptic patterns and their corresponding impacts on clouds,
137 aerosols, radiation, and PBL. Finally, the conclusions are presented in Section 5.

138 **2 Data and method**

139 **2.1 Observation data**

140 Air quality monitoring data used in this study were obtained from air quality monitoring sites
141 established by the Ministry of Ecology and Environment of China across the SCB. Hourly PM_{2.5}
142 observations from 18 stations in the SCB were collected during the winter period from 2015 to 2021
143 for data analysis and model verification purposes (Fig. 1b). The abbreviations CQ, CD, MY, DY,
144 LS, MS, YA, ZY, ZG, YB, LZ, NJ, GA, NC, SN, GY, DZ, and BZ represent the following cities:
145 Chongqing, Chengdu, Mianyang, Deyang, Leshan, Meishan, Yaan, Ziyang, Zigong, Yibin,
146 Luzhou, Neijiang, Guangan, Nanchong, Suining, Guangyuan, Dazhou, and Bazhong, respectively.

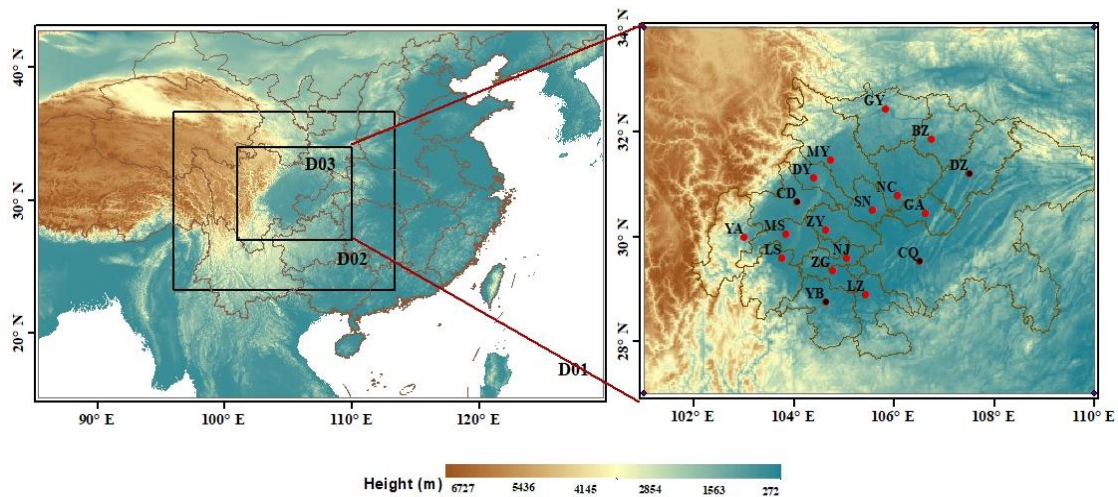


Figure 1. (a) Three layers of simulation domains in WRF-Chem with topography map as shading; (b) the locations of 18 air quality monitoring stations (red dots) and 4 sounding stations (black dots) in the Domain 3.

147

148 The SCB has four sounding stations: Wenjiang (CD), YB, DZ, and Shapingba (CQ), situated in
 149 the western, southern, northwestern, and eastern regions of the basin, respectively (Fig. 1b), and
 150 represent different pollution and meteorological conditions in different regions within the SCB. In
 151 all, the air pollution over the SCB exhibits a gradual decrease from southwest to northeast.
 152 Statistical analysis indicates that the western and the southern basin experience the most severe
 153 pollution. The western basin shows the highest pollution proportion, while the southern basin
 154 exhibits the highest occurrence of heavy pollution. In the northeastern basin, specifically in DZ,
 155 heavy pollution is more likely to occur during winter, which verifies it to be the third highest
 156 pollution zone outside the western and southern basin. This makes the spatial distribution during
 157 winter differs from the overall annual pollution pattern in the SCB (Lu et al., 2022; Qi et al., 2022).
 158 Regarding meteorological conditions, research reveals that DZ has the lowest ventilation
 159 coefficient during winter, while CQ has the highest. The SCB experiences frequent temperature
 160 inversions, with CD having a higher occurrence of inversions compared to the other three cities.
 161 CD also exhibits the strongest inversion intensity and is prone to multi-layer inversions. On the
 162 other hand, YB and CQ have greater inversion thickness, while CD has the smallest inversion
 163 thickness (Feng et al., 2020). The vertical distribution of the meteorological factors used in the
 164 study was obtained from an L-band sounding radar, collecting temperature, pressure, humidity,
 165 and wind data at 00:00 and 12:00 Coordinated Universal Time (UTC) on vertical levels every
 166 second from the surface up to 30 km. Ground observation data from the four cities, including
 167 temperature and dew point temperature, were used for meteorological factor simulation verification.
 168 All meteorological data were obtained from the China Weather Website Platform maintained by
 169 the China Meteorological Bureau. As for the calculation of PBLH, there are various methods to
 170 determine the PBLH, and differences in methods, data or threshold values may yield quite
 171 different PBLH results (Seibert et al., 2000; Eresmaa et al., 2006; Jiang et al., 2021). The bulk

172 Richardson number (Ri) method was adopted to calculate the PBLH with sounding data in
173 the study by assuming that the PBLH is the height at which Ri reaches its critical value (Rc).
174 Ri at a certain height h is calculated as follows:

$$175 \quad Ri = \frac{(g / \theta_{v0})(\theta_{vh} - \theta_{v0})h}{u_h^2 + v_h^2}$$

176 Where g is the acceleration of gravity, θ_{v0} and θ_{vh} are the virtual potential temperature at surface
177 and the height h , respectively, and u_h and v_h are the meridional and zonal wind components at h .
178 We adopted the Ri method and Rc to be 0.25, because the EAR5 and YSU schemes use the same
179 method and threshold value when calculating PBLH (Hong et al., 2006; ECMWF, 2017).

180 CD, YB, DZ and CQ were selected as representative cities for analysis in the study. These four
181 representative cities are located in the western, southern, northwestern, and eastern regions of the basin,
182 to capture diverse pollution and meteorological conditions within the SCB. These cities were chosen to
183 represent the most polluted regions (Zhao et al., 2018; Lu et al., 2022), as well as typical basin and
184 mountainous cities. Furthermore, there are only four sounding stations in the SCB available, which are
185 located in these four representative cities. They can provide valuable vertical and surface
186 meteorological observations, as well as pollution data, contributing comprehensive dataset used in this
187 study.

188 ERA5 reanalysis data from the European Centre for Medium-Range Weather Forecasts (ECMWF),
189 which assimilates comprehensive observation data, including ground observation, sounding data,
190 aircraft observation data, and satellite observation data, were obtained for synoptic pattern
191 classification and their impact on meteorological factors in four representative cities. The EAR5
192 data at the 850 hPa pressure level were collected for the synoptic pattern study. Additionally, cloud
193 liquid water content and downward solar radiation derived from the EAR5 single-level datasets
194 were obtained to assess the influences of synoptic forcing on CRI studies, while PBLH were
195 adopted to conduct the simulation verification. Previous studies have demonstrated the reliability
196 of ERA5 data in estimating cloud properties, including the cloud liquid content (Yao et al., 2019;
197 Nandan et al., 2022; Ojo et al., 2023).

198 **2.2 Synoptic pattern classification**

199 The objective classification was conducted on the synoptic patterns of the SCB using ERA5 data,
200 including geopotential height, u , and v components of winds at the 850 hPa pressure level. The
201 analysis covered an area of 97–117° E and 24–37° N with a horizontal resolution of $0.25^\circ \times 0.25^\circ$.
202 Given that PM pollution in the SCB is primarily prevalent during winter months (Zhao et al., 2018;
203 Lu et al., 2022), the synoptic pattern classification was performed for winter seasons from 2015 to
204 2021 (December, January, and February) using the principal component analysis in the T-model
205 (T-PCA) objective method. Compared with the subjective classification method, the objective
206 method can process large amounts of data without relying on subjective experience (Huth et al.,
207 2008; Miao et al., 2017). Among various classification methods, the T-PCA method accurately

208 reflects the characteristics of the original synoptic circulations and exhibits spatial and temporal
 209 stability (Huth et al., 1996; Huth et al., 2008). Consequently, the T-PCA has been widely used in
 210 synoptic pattern classification researches (Ning et al., 2019; Miao et al., 2020; Li et al., 2021).

211 **2.3 Model configuration and simulation experiments**

212 To understand the combined effects of synoptic patterns and CRI inhibition on ARI and PBL, a
 213 series of parallel experiments were conducted on the simulation of a typical pollution episode
 214 using the Weather Research and Forecasting model with Chemistry (WRF-Chem v3.9.1) (Grell et
 215 al., 2005). The Advanced Research WRF (ARW) dynamics solver integrates the compressible,
 216 nonhydrostatic Euler equations, for example, the momentum equation, the continuity equation, the
 217 thermodynamic equation, the moisture equation and the ideal-gas equation of state (Skamarock et
 218 al., 2008). The model domain (Fig. 1a) was centered over the SCB and utilized three layers of
 219 nested grids with horizontal resolutions of 27, 9, and 3 km, respectively. A total of 32 vertical
 220 layers spanning from the surface to 100 hPa were defined. Initial and boundary meteorological fields
 221 were obtained from the National Centers for Environmental Prediction Final reanalysis data with a
 222 horizontal resolution of $1^\circ \times 1^\circ$ and 6 h time interval. For chemical process simulations,
 223 anthropogenic emissions were sourced from the Multiresolution Emission Inventory for China
 224 (MEIC) in 2016, featuring a grid resolution of $0.25^\circ \times 0.25^\circ$. To address the empirically
 225 overestimated $PM_{2.5}$ emissions by the MEIC in the SCB (Zhan et al., 2023), the ensemble square
 226 root Kalman filter were implemented on the $PM_{2.5}$ emission during simulation (Wu et al., 2018;
 227 Lu et al., 2021). Biogenic emissions were calculated online using the Guenther scheme (Guenther
 228 et al., 2006). Table 1 provides a summary of the chosen physical and chemical parameterization
 229 schemes. The parameterization schemes employed in this study is the one used by the Chongqing
 230 Meteorological Bureau in the daily operational activities. The schemes have been obtained
 231 through multiple sets of control experiments and are considered suitable for the simulation in the
 232 SCB.

233 **Table 1 The main options of WRF-Chem**

Items	Contents
Domains (x, y)	(155, 110), (184, 160), (320, 250)
Grid spacing (km)	27, 9, 3
Center	(29.1° N, 106.2° E)
Time step (s)	60
Microphysics	WRF Single-Moment 5 class (WSM5) scheme
Longwave radiation	RRTMG scheme (Iacono et al., 2008)
Shortwave radiation	RRTMG scheme (Iacono et al., 2008)
Planetary boundary layer	Younsei University scheme (Hong et al., 2006)
Land surface	United Noah land surface model (Tewari et al., 2004)
Cumulus parameterization	Grell-Freitas ensemble scheme

	(Grell et al., 2013)
Advection	fifth- and third-order differencing for horizontal and vertical advection respectively
Photolysis scheme	Fast-J photolysis (Fast et al., 2006)
Gas-phase chemistry	RADM2 (Stockwell et al., 1990)
Aerosol module	MADE/SORGAM (Schell et al., 2001)

234

235 To assess the impact of CRI inhibition on ARI under typical synoptic pollution patterns, four
 236 parallel experiments were conducted using simulation models. The selected simulation period for
 237 these experiments was January 1-7, 2017. The period was selected for two reasons: the Chinese
 238 government announced clean-air action in the year of 2013, aiming to reduce PM_{2.5} concentrations in
 239 the next 5 year. Specifically, the year of 2017 was identified as a key year for assessing PM_{2.5} pollution
 240 in China, as significant practical actions were implemented during the period (Wang et al., 2020) and
 241 the selected period encompassed both typical pollution and clean weather patterns.

242 The baseline experiment (BASE) included both CRI and ARI in the simulations. In contrast, the
 243 three sensitivity experiments focused on excluding either ARI or CRI. Experiment 1 (EXP1) did not
 244 consider ARI, Experiment 2 (EXP2) did not include CRI, and Experiment 3 (EXP3) omitted ARI
 245 when CRI was not included. The differences between BASE and EXP1 represented the
 246 disturbances caused by ARI, while EXP2 and EXP3 represented the influences of ARI without
 247 CRI inhibition. Detail differences between the experiments could be found in Table 2. The
 248 numerical experiments were initiated at 00:00 UTC on December 30, 2016, and ran until 00:00
 249 UTC on January 8, 2017, with the first 48 hours designated as a model spin-up period.

250 **Table 2 Four numerical simulation experiments are conducted in the study**

Experiments	Description	Results	Meaning
BASE	Baseline simulation	BASE-EXP1	Disturbances by ARI
EXP1	Only shutting down ARI		
EXP2	Only shutting down CRI	EXP2-EXP3	Influences of ARI without CRI
EXP3	Shutting down both ARI and CRI		

251 *ARI: aerosol radiation interaction; CRI: cloud radiation interaction

252 **3 Results and discussions**

253 **3.1 Relationships between synoptic patterns and PM_{2.5} pollution in the SCB**

254 Figure 2 illustrates the daily mean variations in PM_{2.5} concentration and vertical distributions
 255 of potential temperature (PT) during winter period from 2015 to 2021, with a focus on the pollution
 256 episodes. The four sounding stations located in separate areas of the SCB (CD, YB, CQ, and DZ),
 257 consistently experienced pollution processes characterized by simultaneous changes in vertical
 258 thermal structures. For example, during the pollution events in January 2017 and December 2020,

259 the PM_{2.5} concentrations in all four cities reached their peak levels at the same time before rapid
 260 declining (Fig. 2). Interestingly, these pollution episodes were accompanied by warming in the
 261 upper layer atmosphere, while a decrease in PM_{2.5} concentration correlated with cooling. Despite
 262 the significant distances between these cities (approximately 200–400 km), the synchronized
 263 changes in pollutant concentrations and vertical thermal structures could be attributed to large–
 264 scale synoptic patterns (Miao et al., 2020; Li et al., 2021). While the four cities with sounding
 265 stations were selected as representatives for vertical thermal structure analysis, other cities in the
 266 SCB also experienced pollution episodes and relevant physical processes, except for GY (Fig. S1).
 267 GY is located in the northern edge of the SCB, bordering Shaanxi and Gansu Provinces. The proportion
 268 of heavy PM_{2.5} pollution in GY is the lowest in the basin, but the proportion of PM₁₀ pollution is higher
 269 than other cities of SCB (Lu et al., 2022). Due to the lower PM_{2.5} concentration, the two pollution
 270 processes in January 2017 in GY were not as significant as in other cities within the basin. However,
 271 the warming of upper air coincided with PM_{2.5} increase could still be observed.

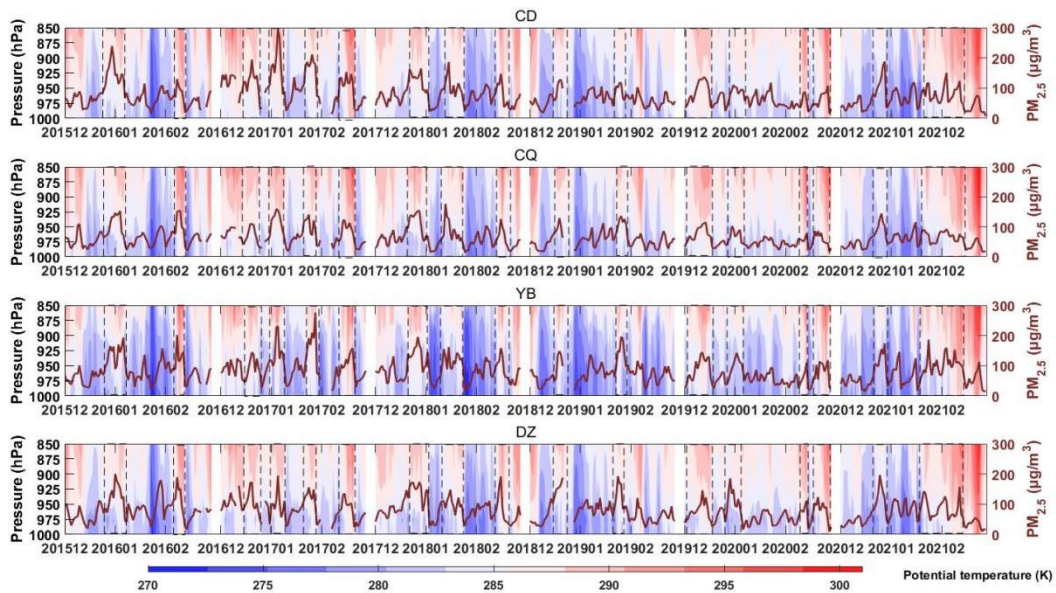


Figure 2. Time series of daily mean PM_{2.5} and potential temperature derived from the sounding data during 2015–2021 winter months. The PM_{2.5} pollution episodes are marked with black dotted boxes.

272

273 The time series of daily mean PM_{2.5} from air quality monitoring sites and the accompanying
 274 vertical distributions of temperature, relative humidity, and wind in CD, CQ, YB, and DZ derived from
 275 the sounding stations are shown in Fig. S2, focusing on January 2017 as an example for analysis.
 276 During this month, two severe PM_{2.5} pollution episodes occurred: one from January 1 to 7 and another
 277 from January 24 to 31 in 2017. These pollution episodes had a significant impact on air quality in all
 278 four cities. The highest daily PM_{2.5} concentrations recorded during these episodes were 291.17 µg/m³ in
 279 CD and 276.2 µg/m³ in YB. Pollution in early January exhibited a gradual increase in PM_{2.5} levels from
 280 January 1 to 3, with upper air warming and the emergence of an inversion above the PBL. Additionally,
 281 lower humidity and higher wind speeds above 1500 m were observed during the pollution
 282 accumulation period. Similarly, the late January pollution episode showed a rapid increase in PM_{2.5},
 283 from January 24 to 27, together with warming, dryness, and high wind speed above 1500 m in all four

284 cities. These consistent meteorological conditions during the pollution periods indicated significant
285 synoptic forcing. The previous study has found that winter heavy pollution processes in the SCB are
286 usually associated with abnormal warming above the 850 hPa (Lu et al., 2022). The warming is
287 induced by strong southerly airflow above the basin. The southerly airflow in winter over the SCB
288 originates from the Yunnan-Guizhou Plateau or the Indian Peninsula, characterized with high
289 temperature, dryness, and high wind speed. The strong southerly airflow forms a warm lid over the
290 basin, suppressing the vertical exchange of pollutants within the basin. As a result, pollutants
291 accumulate rapidly, which may explain the phenomenon of rapid PM_{2.5} growth accompanied by
292 warming, dryness, and strong winds above 1500 m. Notably, the key layer for studying the connection
293 between synoptic patterns and PM_{2.5} pollution is approximately 850 hPa, corresponding to a height of
294 approximately 1500 m within the PBL, where changes in specific meteorological conditions primarily
295 affect surface-emitted pollutants.

296 Using ERA5 reanalysis data for winter (December, January, and February) from 2015 to 2021,
297 the 850 hPa synoptic patterns over the SCB were objectively classified into six types (Fig. 3).
298 According to the relative positions of the high-pressure and low-pressure systems in the basin,
299 these synoptic patterns could be described as follows: (1) strong high pressure in the north, (2) east
300 high west low (EHWL) pressure, (3) weak high pressure in the north, (4) weak ridge of high
301 pressure after the trough, (5) low trough (LT), and (6) strong high pressure. Patterns 1 and 3
302 exhibited high pressure in the northern SCB, which differed from the high-pressure intensity. With
303 strong high pressure, the basin was primarily controlled by northerly airflow. Under weak high-
304 pressure conditions, the basin was dominated by an easterly backflow. Patterns 2 and 5 had high
305 and low pressures near the basin, forming a relatively dense isopotential altitude gradient and
306 resulting in strong southerly winds over 850 hPa. Pattern 4 was a weak high-pressure ridge after a
307 trough controlled the SCB with sparse isobaric lines and weak winds leading to static and stable
308 weather conditions. During Pattern 6, the SCB was controlled by the cold high-pressure system,
309 accompanying weak northerly airflow on the basin. Pattern 6 usually evolved from either Pattern 1
310 or Pattern 3.

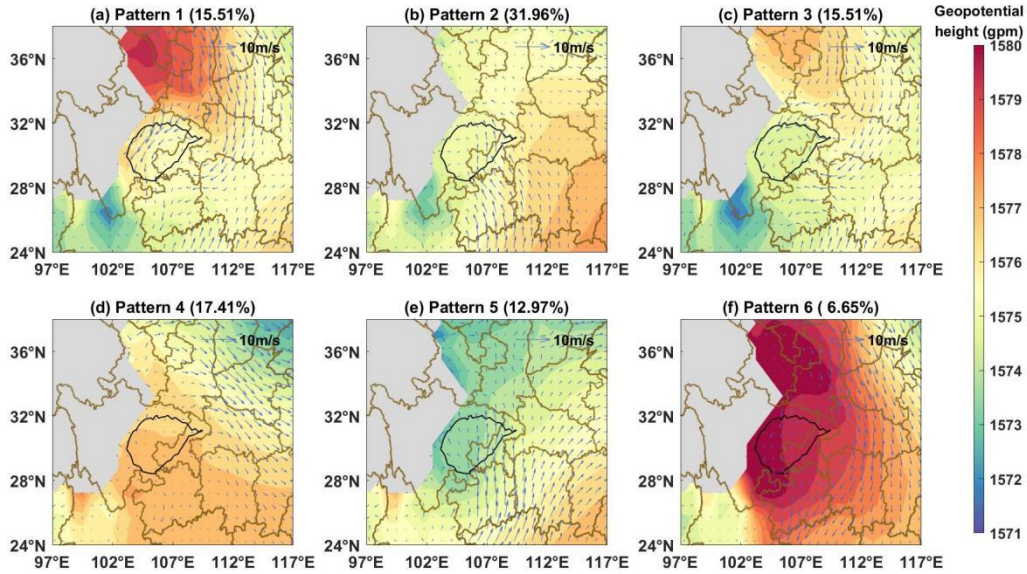


Figure 3. The 850hPa geopotential height field (shading) with wind vector fields (blue vectors), and frequency of occurrence for 6 synoptic patterns during 2015-2021 winter months. The SCB was outlined with an altitude contour of 750 m terrain height (black lines).

311

312 Patterns 2, 4, and 5 exhibited higher frequencies of pollution occurrence ($PM_{2.5}$ daily
 313 concentration $\geq 75 \mu\text{g}/\text{m}^3$) according to statistical results from 18 cities in the SCB during the
 314 2015–2021 winters (Fig. 4a). These patterns were associated with high $PM_{2.5}$ concentrations in 50–
 315 70 % days, including CD, DY, and MY in the northern SCB, 40–60 % for cities in the southern
 316 SCB, such as ZG and YB, and also 40–60 % of days for cities in the northern SCB, such as CQ, DZ,
 317 NC, and GA. Furthermore, the average $PM_{2.5}$ concentrations in the respective cities for the six
 318 synoptic patterns were calculated (Fig. 4b), aligning with the frequency of pollution occurrence.
 319 The days under Patterns 2, 4, and 5 exhibited higher average daily $PM_{2.5}$ concentrations. The average
 320 concentrations under these three synoptic patterns were 99.19, 103.43, and 111.97 $\mu\text{g}/\text{m}^3$ for CD,
 321 95.44, 87.98, and 94.26 $\mu\text{g}/\text{m}^3$ for YB, 79.14, 83.96, and 74.77 $\mu\text{g}/\text{m}^3$ for CQ, and 91.02, 104.64,
 322 and 91.51 $\mu\text{g}/\text{m}^3$ for DZ, respectively. Regarding the impact of synoptic patterns on the
 323 accumulation or dispersion of $PM_{2.5}$, Fig. 4c illustrates the average daily changes in $PM_{2.5}$
 324 concentration compared with the previous day for CD, CQ, YB, and DZ under the six synoptic
 325 patterns. Patterns 2 and 5 exhibited the most significant $PM_{2.5}$ accumulation under the influence of
 326 southerly airflow. The average $PM_{2.5}$ concentration under Pattern 1, 3 and 6 was lower in all cities
 327 of SCB than other three pollution patterns (Fig. 4a). Besides, the day to day $PM_{2.5}$ variations under
 328 Pattern 1, 3 and 6 exhibited negative growth trend in the four representative cities (Fig. 4c). As a
 329 result, Pattern 1, 3 and 6 were identified as the “clean pattern”. In addition, the pollution
 330 occurrence frequency of which was found higher for cities located in the eastern part of the SCB
 331 than other parts. Under Pattern 6, strongest northerly airflow affects the basin. The eastern part of
 332 the basin consists of parallel ridges and valleys, which reduces wind speed. The stronger the wind
 333 is, the more obvious the reduction of wind by terrain is. In contrast, the western part is relatively
 334 flat, which can result in higher surface wind speeds. The difference in wind impacted by terrain

335 led to a weaker pollution removal effect in the eastern region, thus contributing to a higher
 336 proportion of pollution days under Pattern 6. Besides, differences in precipitation rates between
 337 eastern cities and other regions were not significant (the proportion of rainfall with a daily
 338 accumulated precipitation exceeding 10 mm in CD, CQ, YB and DZ under Pattern 6 were all less than
 339 3%) , which might not the main reason why eastern cities in the SCB experience higher pollution
 340 frequency.

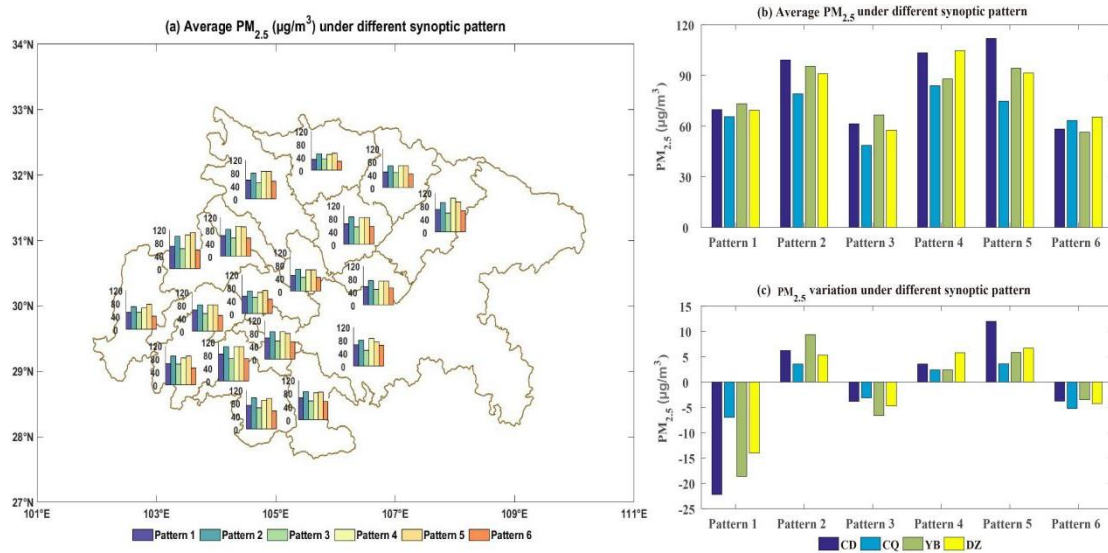


Figure 4. (a) The pollution occurrence frequency at 18 air pollution stations in SCB, (b) (c) average PM_{2.5} concentrations and PM_{2.5} day to day variations at 4 representative SCB cities, under 6 synoptic patterns.

341

342 The time series of daily mean PM_{2.5} and the day-to-day classification of 850 hPa synoptic
 343 patterns are shown in Fig. S3, from December 2016 to January 2017. Six pollution episodes
 344 occurred during this period (December 03–12 and 16–26, 2016; January 1–7, 16–19, and 20–28,
 345 2017; and February 14–23). It is observed that pollution episodes consistently began with Pattern 2
 346 and ended with Pattern 1, accompanied by a rapid decline in PM_{2.5}. This finding suggests that
 347 Pattern 2 acted as a key synoptic forcing for the initiation of pollution episodes. Additionally,
 348 statistical results revealed that Pattern 2 accounted for a high proportion of PM_{2.5} increase during the
 349 six pollution episodes, reaching 48.48 %, while Pattern 5 had the second highest proportion of
 350 21.88 %, with Patterns 2 and 5 combined accounting for more than 70 % of the pollution episodes.
 351 For example, during the two heavy pollution events in early and late January 2017, PM_{2.5} rapidly
 352 accumulated with the interplay of Patterns 2 and 5. These two patterns represented a substantial
 353 proportion of 31.96 % and 12.97 %, respectively, during winters from 2015 to 2020 at 850 hPa
 354 level in the SCB (Fig. 3). Based on this analysis, Patterns 2, 4, and 5 were identified as synoptic
 355 pollution patterns, whereas Patterns 1, 3, and 6 were as clean patterns. In summary, Patterns 2 and
 356 5 played crucial roles in the initiation and accumulation of PM_{2.5} during pollution episodes.

357 The discussion above showed that pollution in the SCB tended to occur when southerly airflow
 358 controlled the upper-layer of the basin (Pattern 2 and 5), while the dispersion of pollutants was

359 accompanied by northerly winds, which aligns with the findings of Lu et al. (2022). This study
360 indicated that southerly airflow in the upper-layer could bring warm air, leading to warming above
361 the basin and forming a “warm lid”. The surrounding mountains and plateau with the “warm lid”
362 contributed to the formation of a relative enclosed space within the SCB, facilitating local
363 circulations and allowing for the thorough mixing and secondary reactions of local emission and
364 pollutants transported from outside. As a result, persistent and severe pollution often occurred
365 under the influence of southerly airflow. When the northerly airflow began to dominate the SCB,
366 the “warm lid” and local circulation were disrupted, leading to dispersion of pollutants through
367 advection and vertical transport. Northerly winds were often associated with cold air and
368 sometimes accompanied by weak precipitation, resulting to wet deposition and the removal of
369 pollutants. Therefore, the arrival of northerly airflow often signified the ending of the pollution
370 episode. The evolution of 850 hPa synoptic forcing and vertical meteorological conditions (Fig. 2
371 and 6) aligns with the study of Lu et al (2022). Therefore, there are also similar pollution change
372 mechanisms.

373 Due to the convergence of air moving eastward across the Tibetan Plateau, the SCB experiences
374 frequent wet and cloudy weather, with cloud cover fraction exceeding 80 % (Yu et al., 2004;
375 Zhang and Lin, 1985). Clouds undoubtedly play an unneglectable role in the interactions of
376 aerosols, radiation, and the PBL under typical synoptic forcing in this region. This study evaluated
377 the average cloud liquid water content, downward solar radiation, and PBL under the influence of
378 the six classified synoptic patterns in CD, CQ, DZ, and YB, using data from ERA5 (Fig. 5). The
379 reanalysis data revealed significant higher cloud liquid water contents with Patterns 2 and 5, likely
380 triggered by robust southerly air prevailing at 850 hPa over the SCB (Fig. 3). This southerly air
381 brought warm and moist air, contributing to cloud formation. Dense clouds reduced solar radiation
382 through reflection and scattering, resulting in surface cooling and inhibiting PBL development.
383 The PBLH under Patterns 2 and 5 was approximately 900–1000 m, lower than that under the
384 influence of clean synoptic Pattern 6 at 1500 m or Pattern 1 and 3 at 1200–1300 m (Fig. 5). In
385 contrast, the clean synoptic Pattern 1 was characterized by a strong northerly flow at 850 hPa,
386 resulting in lower cloud liquid water content over the basin and increased solar radiation, promoting
387 PBL development. The lower PBLH with more stable stratification caused by the CRI in Patterns 2
388 and 5 could partially explain the rapid accumulation of $PM_{2.5}$ during these two pollution patterns.
389

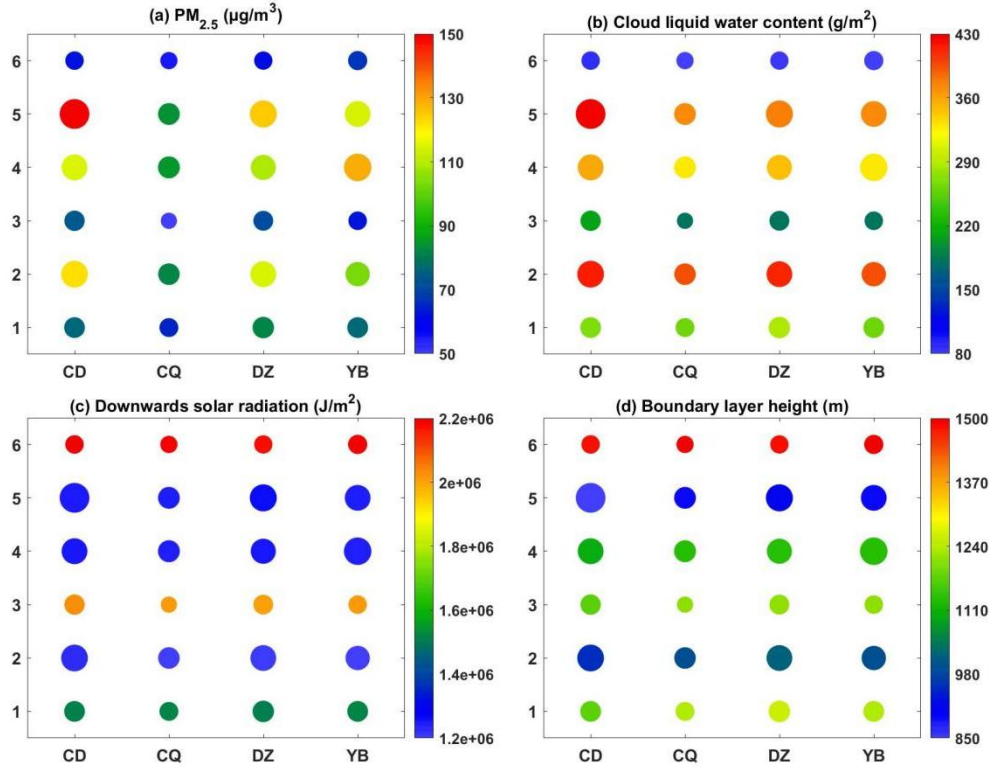


Figure 5. The averaged (a) PM_{2.5} concentrations, (b) cloud liquid water contents, (c) downwards solar radiation and (d) boundary layer height derived from 2015-2021 winter months ERA5 reanalysis data, at 4 representative SCB cities under 6 synoptic patterns, the dot sizes represent PM_{2.5} concentrations.

390

391 3.2 Integrate impacts of synoptic patterns and the CRI inhibition on ARI

392 Based on the above analysis, Patterns 2 and 5 were identified as the key pollution synoptic
 393 patterns accompanying dense clouds and, thus, strong CRI. However, the effects of pollution
 394 patterns on ARI and their interaction with CRI in the SCB remain unclear and warrant further
 395 investigation. A typical pollution episode from January 1–7, 2017, was selected to understand these
 396 complex processes and simulated using WRF–Chem. The BASE simulations were verified with
 397 observations to determine the accuracy and reliability of the simulation results. The simulation and
 398 observation of PM_{2.5}, T₂, TD₂ and wind speed values with some statistical metrics in CD from
 399 January 1–7 are shown in Fig. 6a-d. Similar information at CQ, YB and DZ can be found in the
 400 Fig. S4. The MB of the simulated and observed PM_{2.5} concentrations were -15.59, -13.42, 2.10
 401 and -13.11 µg/m³, with NMB values of -4.12%, -4.22%, 6.01% and -0.68% at four cities,
 402 respectively, which are within the acceptable standards (NMB < ± 15%). The R of PM_{2.5} were
 403 78.91%, 57.23%, 61.15% and 62.86% for four representative cities, respectively. The statistical
 404 metrics for PM_{2.5} are consistent with previous studies (Wang et al., 2020; Shu et al., 2021; Zhan et
 405 al., 2023), indicating that our model results for PM_{2.5} are reasonable and acceptable. Regarding to
 406 the surface meteorological factors, low MB and high R for both temperature and dew point

407 temperature suggested good simulation performance for these variables. However, the simulation
408 results for wind speed were poor, which was expected under conditions of low wind and complex
409 terrain. The high observed calm wind frequency, influenced by the starting speed of the
410 anemometer, led to an overestimation in the simulation (Shu et al., 2021; Zhan et al., 2023).
411 Additionally, it could be argued that unresolved topographic features introduce additional drag,
412 beyond that generated by vegetation, which was not considered in the WRF model (Jimenez and
413 Dudhia, 2012).

414 In addition, the temporal averaged and variations of vertical profiles for potential temperature,
415 relative humidity and wind speed in the model were compared with the sounding data in CD (Fig.
416 6e-m). Model evaluation of vertical structures in CQ, YB and DZ can be found in Fig. S5. The
417 SCB is characterized with cloudy and foggy conditions, which result in abundant water vapor and near
418 100% relative humidity above the nocturnal boundary layer. Models often underestimate the humidity
419 above the boundary layer during night in the SCB (Shu et al., 2021). Furthermore, due to complex
420 terrain and measurement bias of the anemometer for weak winds, the evaluation of simulation results
421 for wind speed often exhibit certain deviations (Jimenez and Dudhia, 2021; Shu et al., 2021; Zhan et al.,
422 2023). For the verification of PBLH, sounding data are commonly regarded as reliable vertical
423 observation records, and PBLH calculated based on sounding data can be used as the true values to
424 compare with other data for long-term validation (Guo et al., 2016). However, for short-term studies,
425 due to limited availability of sounding data at only 00:00 and 12:00 UTC, the ERA5 data were also
426 incorporated for the model evaluation of PBLH in this study (Fig. 6 and Fig.S5). The simulation PBLH
427 showed a consistent trend with those calculated from ERA5 and sounding data. Overall, the simulation
428 results can capture the meteorological and PM_{2.5} variation trends. According to the simulation
429 evaluation standards for the SCB in previous studies (Wang et al., 2020; Zhan et al., 2023), the results
430 is acceptable and reasonable; thus, the simulation can be used for subsequent analysis and discussion.

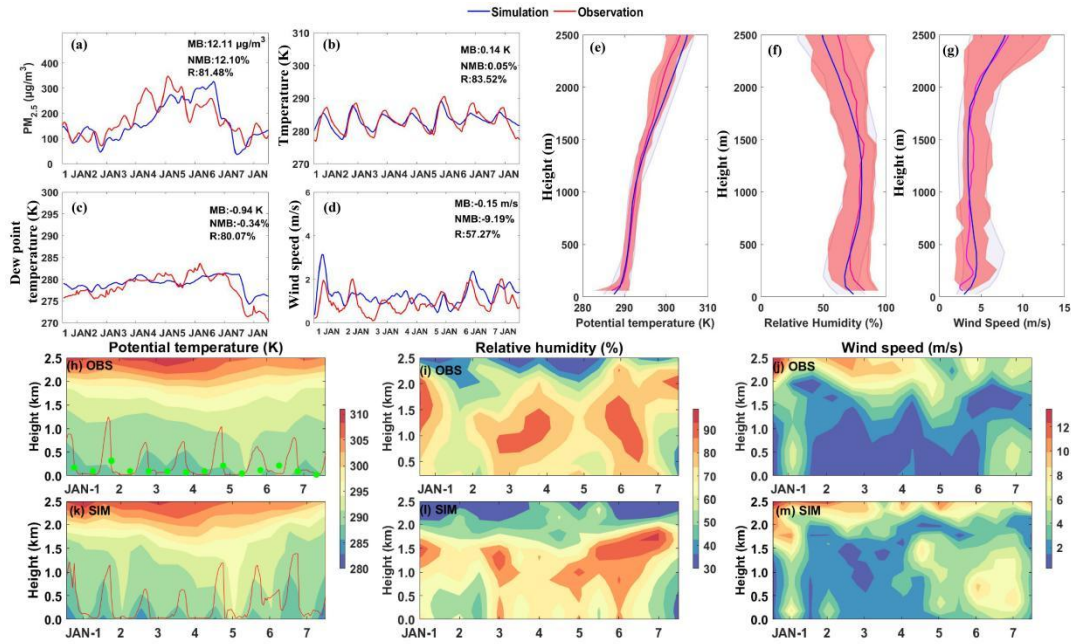


Figure 6. Time series of hourly simulated and observed (a) $PM_{2.5}$ concentration, (b) temperature at 2 m, (c) dew temperature at 2m and (d) wind speed near surface, and comparison of simulated and observed mean vertical profile of (e) potential temperature, (f) relative humidity and (g) wind speed, the red and grey shaded areas represent deviations to the mean values of observation and simulation, respectively. The simulated and observed time-height sections of (h)(k) potential temperature, (i)(l) relative humidity and (j)(m) wind speed are also given, while the red lines in (h)(k) are time series the boundary layer heights derived from ERA5 data and simulation with green dots representing boundary layer heights calculated with sounding data. The above figures display information in CD. Additionally, the model verification information regarding CQ, YB and DZ can be found in Supplement Figure 3 and 4.

431

432 During the pollution episode that occurred from January 1 to 7, 2017, the pollution synoptic
 433 patterns controlled the SCB as follows: Pattern 2 from January 1 to 3, Pattern 5 from January 4 to 6,
 434 and Pattern 1 on January 7. Consequently, $PM_{2.5}$ pollution in the SCB occurred on January 1–6 and
 435 rapidly dissipated on January 7 (Fig. 7). The mean geopotential height at 850 hPa derived from the
 436 simulation of January 1–3 under Pattern 2 showed EHWL, with southerly flow prevailing over the
 437 SCB (Fig. 7a). The resulting upper air warming suppressed PBL development (Fig. 7d). During
 438 January 1–3 under Pattern 2, the average PBL heights were lower (Fig. 7d), acting as a lid above the
 439 SCB and hindering the airflow within the basin due to the surrounding mountains. Low wind
 440 speeds provided adverse diffusion conditions for pollutants emitted into the basin, resulting in
 441 severe pollution in the western and southern SCB (Fig. 7g). From January 4 to 6, the low pressure
 442 over the SCB evolved into a LT pattern, termed Pattern 5 in the previous analysis. Compared with
 443 Pattern 2, the isobaric lines were denser under the influence of the LT, leading to stronger southerly
 444 winds above the SCB (Fig. 7a–b). Lower average PBL heights were observed during January 4–6

445 under Pattern 5 compared with those of January 1–3 under Pattern 2 (Fig 7d–e), primarily due to
 446 stronger upper air warming and more stable stratification. Pollutants that accumulated during
 447 January 4–6 from the earlier pollution episode (January 1–3) further increased (Fig. 7g–i). On
 448 January 7, high pressure in the north dominated the SCB, with a prevailing northerly flow over the
 449 basin (Fig. 7c). The PBL height quickly increased due to upper-layer cold advection (Fig. 7f),
 450 resulting in a rapid decrease in $PM_{2.5}$ (Fig. 7i). Overall, synoptic patterns play a key role in the
 451 accumulation and diffusion of $PM_{2.5}$ during pollution episodes by modulating PBL development
 452 and stratification stability.

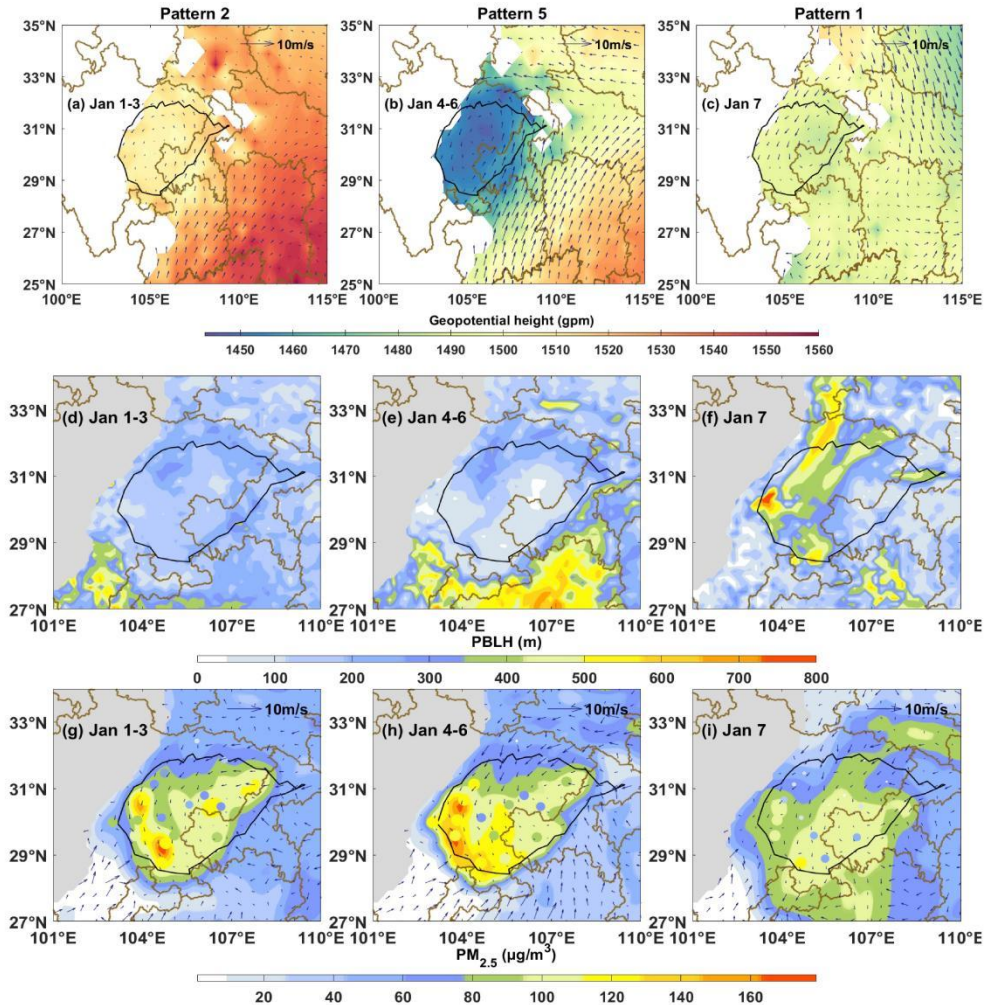


Figure 7. The simulated (a)-(c) 850 hPa geopotential height field (shading) with wind vector fields (blue vectors), (d)-(f) boundary layer height and (g)-(i) $PM_{2.5}$ concentrations (shading) and wind vector fields at 900hPa (blue vectors) for 1-3, 4-6 and 7 January. The size and color of scatters in (g)-(i) show corresponding observed $PM_{2.5}$ concentrations at 18 air quality monitoring stations. The SCB was outlined with an altitude contour of 750 m terrain height (black lines).

453

454 Pollutant accumulation can regulate the PBL structure through the ARI, further exacerbating
 455 pollution (Wang et al., 2018; Miao et al., 2020). In the SCB, this positive feedback is weaker than
 456 in the other regions and may be inhibited by cloud radiation (Zhong et al., 2019). A series of
 457 simulation experiments were conducted to investigate the aerosol radiation feedback in the SCB

458 under the influence of two typical synoptic pollution patterns, as described in Section 2.4. BASE-
 459 EXP1 represents the perturbations caused by ARI, whereas EXP2-EXP3 demonstrates changes
 460 through ARI without CRI inhibition. Aerosols led to surface cooling through absorbing and
 461 scattering solar radiation, thereby inhibiting the development of the PBL, which in turn facilitated
 462 pollutant accumulation (Fig. 8). Compared with Pattern 2, the aerosol concentrations in Pattern 5
 463 were higher, resulting in greater reduction of downward solar radiation reduction due to ARI,
 464 leading to more pronounced cooling near the ground and a lower PBLH. Overall, the ARI in Pattern
 465 5 was more significant than that in Pattern 2, regardless of CRI inhibition (Fig. 8).

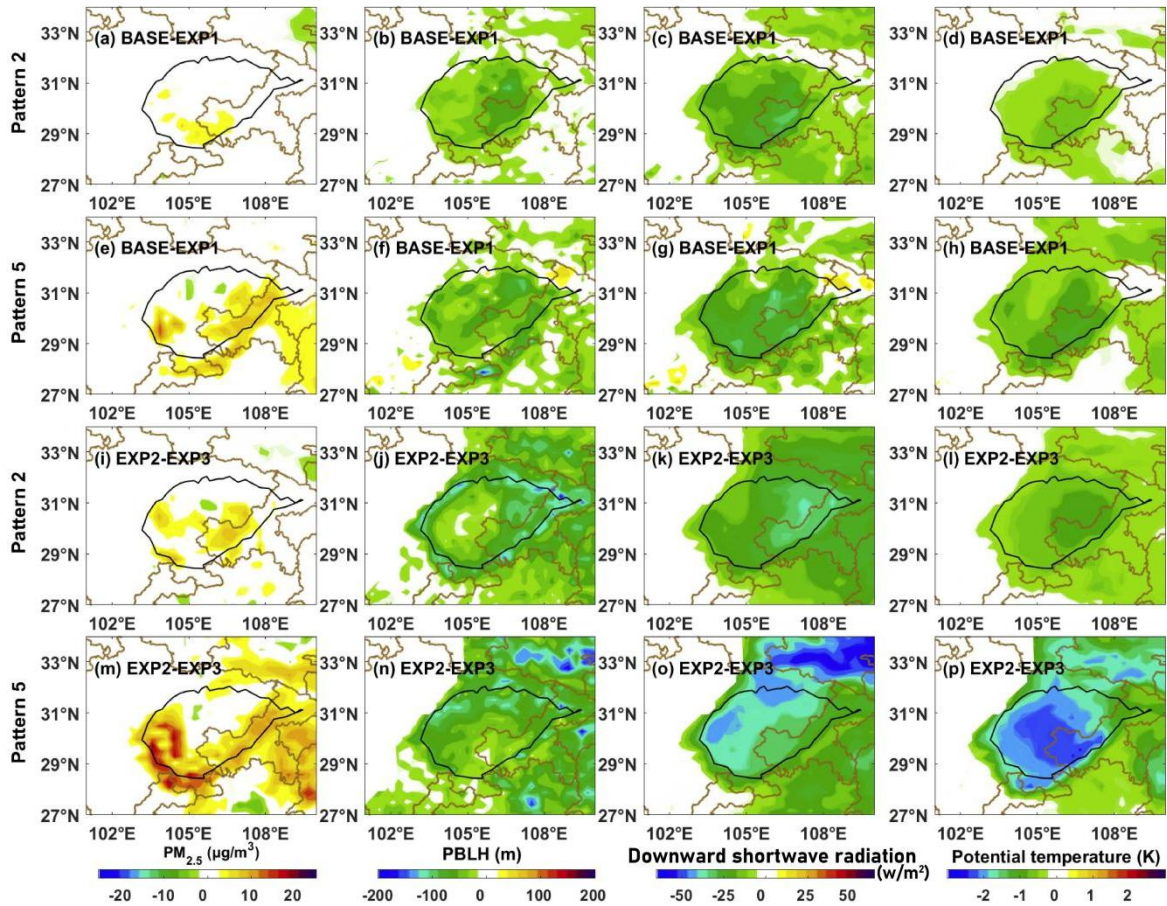


Figure 8. Spatial distribution of perturbations induced by (a)-(h) aerosol radiation interactions (ARI), and (i)-(p) ARI without the cloud radiation interaction (CRI) inhibition during 1-3 and 4-6 January representing Pattern 2 and Pattern 5 synoptic forcing, respectively. The SCB was outlined with an altitude contour of 750 m terrain height (black lines).

466

467 Furthermore, parallel simulation experiments revealed that the CRI significantly attenuated the
 468 ARI in the SCB under both pollution synoptic patterns. When the CRI was not considered, more
 469 solar radiation penetrated the PBL. Dense aerosols accumulated near the surface, intercepting more
 470 downward shortwave radiation, and resulting in stronger cooling near the ground. This suppressed
 471 the development of the PBL, and contributed to a more remarkable ARI (Fig. 8). Regarding the
 472 horizontal spatial distribution, a strong ARI was primarily observed in CQ, as well as in the western
 473 and southern SCB, despite CQ experiencing lower pollutant concentrations compared to the other

474 two regions (Figs. S4 and 7). This weaker ARI phenomenon in the western SCB was also reported
475 by Zhong et al. (2019) and was attributed to CRI inhibition on ARI. Considering the statistical
476 results in Fig. 5, the average cloud liquid water content in CD and YB was significantly higher than
477 that in CQ under the influence of Patterns 2 and 5. Consequently, a more remarkable CRI
478 inhibition on the ARI would occur in the western and southern SCB compared to CQ, leading to a
479 relatively weaker ARI distribution in these regions. Without considering the CRI, the ARI in the
480 western and southern SCB would be much more pronounced than that in CQ. As for the
481 northwestern SCB (DZ), the ARI in DZ is lower than in the other three regions. When the CRI is not
482 considered, the ARI in DZ is higher than in CQ but lower than in CD and YB. This is because DZ has
483 lower aerosol concentrations compared to CD and YB (Fig. 7), but exhibits higher cloud cover than CQ
484 under Patterns 2 and 5 (Fig. 5).

485 Using the western SCB, which exhibited the highest pollution concentration, as an example, Fig.
486 9 illustrates the vertical diurnal variations in temperature and solar radiation caused by the ARI.
487 The results in Fig. 9–11 were derived from the simulation experiments in CD, as CD is one of the
488 most polluted cities with typical meteorological and geographical characteristics of the western SCB.
489 The ARI caused surface cooling in the morning and upper-air warming in the afternoon. As local
490 solar radiation increased from 8 am to 12 pm, the reduction in solar radiation caused by the ARI
491 also increased. Surface cooling reached its peak at approximately 10 am to 12 pm, and gradually
492 weakened in the afternoon. This diurnal variation might be attributed to the enhanced turbulence
493 during morning PBL evolution (Wang et al., 2018). Afternoon surface cooling was partly
494 compensated by the turbulent transport of warm air above the PBL. In addition, strong surface
495 cooling between 5 pm and 8 pm in the SCB, was possibly influenced by remarkable valley wind
496 circulations forced by the Qinghai–Tibet Plateau adjacent to the western SCB (Lu et al., 2022).
497 The evening cooling of the plateau induced strong mountain winds, promoting surface cooling,
498 while the upper-layer warming mainly occurred around 1–1.5 km in the afternoon. In general, the
499 ARI reduces solar radiation, causing surface cooling and upper air warming, thereby regulating the
500 vertical atmospheric thermal structure, suppressing convection, and consequently decreasing PBL
501 heights (Fig. 10).

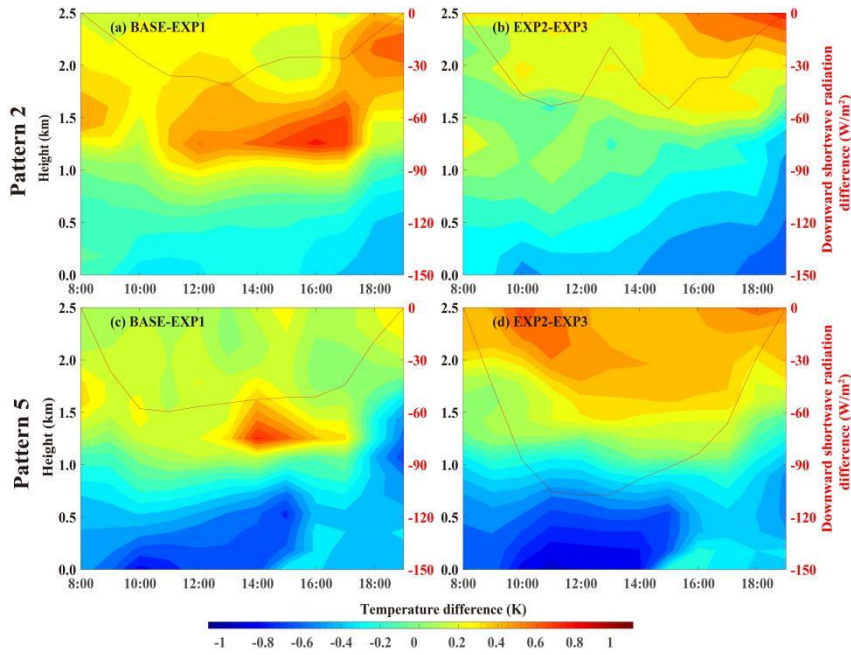


Figure 9. Diurnal variations of vertical temperature perturbations and downward solar radiation under influences of Pattern 2 and Pattern 5 induced by (a) (c) ARI and (b) (d) ARI without CRI inhibition.

502

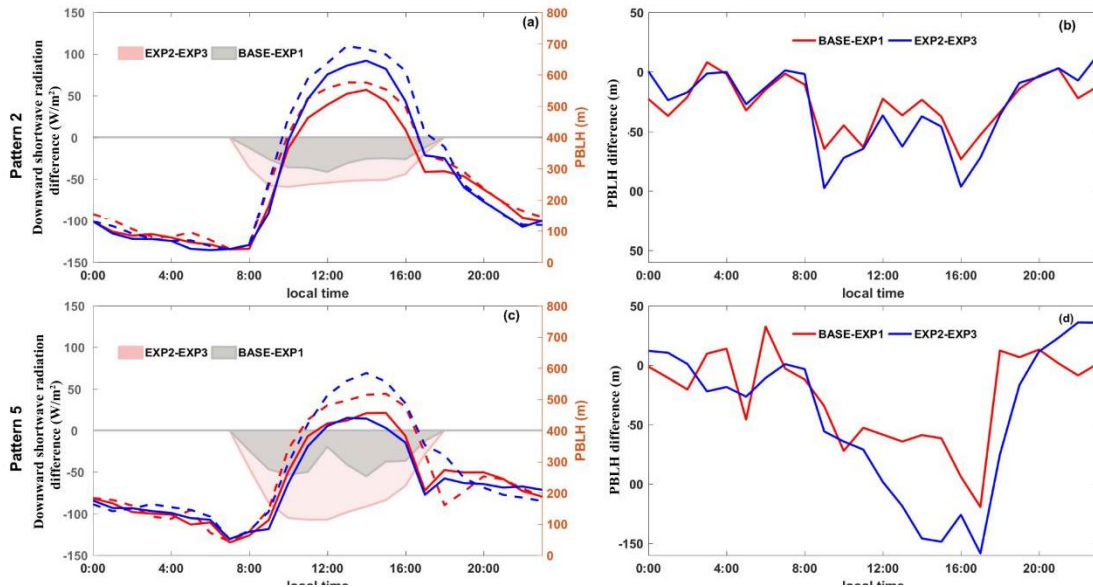


Figure 10. Diurnal variations of (a) (c) boundary layer height(lines) and downward solar radiation(shading), and (b)(d)the perturbations of boundary layer height induced by ARI and ARI without CRI inhibition, under Pattern 2 and Pattern 5 synoptic forcing respectively.

503

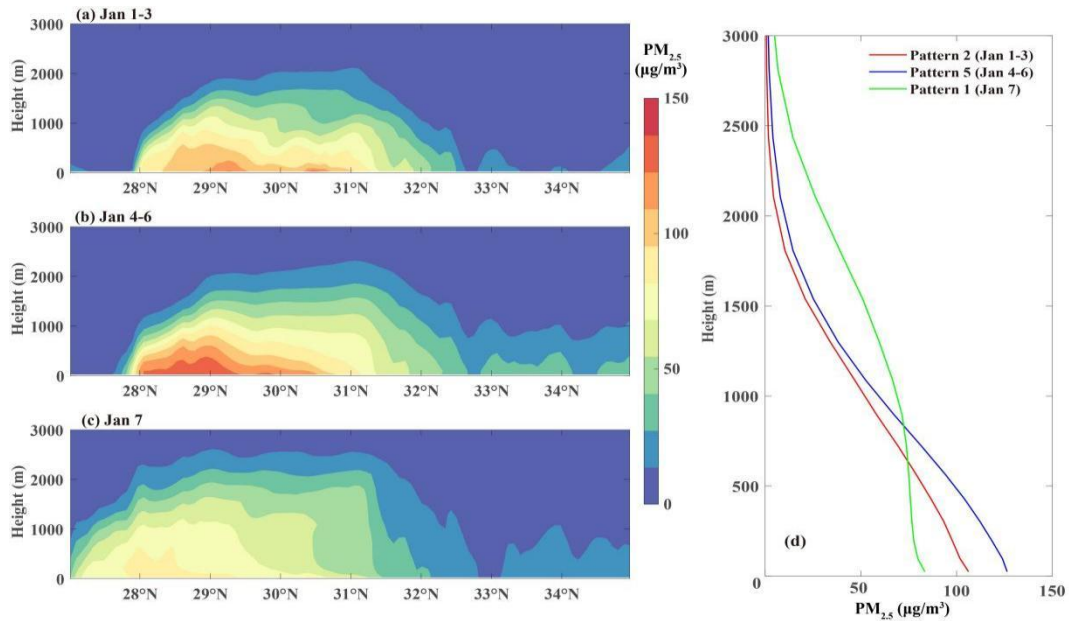


Figure 11. Meridional vertical distribution of averaged PM_{2.5} between 104°E and 105°E under (a) Pattern 2 and (b) Pattern 5, and (c) average profiles of PM_{2.5} within 28°N and 31°N.

504

505 Synoptic patterns play a role in the interaction between the ARI and PBL (Wang et al., 2018;
 506 Miao et al., 2020). Zonal average of PM_{2.5} concentration between 104°E and 105°E was conducted,
 507 and the meridional vertical distribution of PM_{2.5} between 27°N and 35°N was illustrated in Fig.
 508 11a-b. Fig. 11(c) provides an average of PM_{2.5} concentration within 28°N and 31°N, showing the
 509 vertical distribution profiles under Pattern 2 and 5. Due to the inhibition of “warm lid” above the
 510 SCB, the vertical exchange was not prominent under both Pattern 2 and 5, and PM_{2.5} was more
 511 concentrated at the middle and lower levels. The PM_{2.5} concentration under Pattern 5 was higher
 512 than Pattern 2 throughout the atmospheric column, indicating stronger aerosol radiative forcing
 513 and a more significant impact on the boundary layer structure under Pattern 5. During January 4–6,
 514 the surface cooling reached 1 K, with cooling layers higher than those observed on January 1–3.
 515 The differences in thermal structure modulations contributed to a lower diurnal PBLH in Pattern 5
 516 than in Pattern 2 (Figs. 10a and c), indicating that Pattern 5 was more conducive to ARI. Based on
 517 the simulation experiments, this study further discussed the impact of synoptic forcing on the CRI
 518 inhibition of ARI. When the CRI was not considered, the solar radiation reduction at noon on
 519 January 4–6 by the ARI was nearly twice as high as when the CRI was considered.
 520 Correspondingly, surface cooling at noon was remarkably enhanced. In the evening, surface
 521 cooling occurred earlier and was stronger without the CRI (Fig. 9). The regulation of CRI on ARI
 522 was further reflected in changes in PBLH. Without the CRI, the diurnal PBLH increased
 523 significantly, with the PBLH decreased more with ARI without CRI inhibition. The PBLHs were
 524 decreased by the ARI during January 13–17 afternoon, reaching 2–3 times the decrease observed
 525 with CRI inhibition (Fig. 10). More significant CRI inhibition of ARI was revealed under Pattern
 526 5 compared with that under Pattern 2, owing to the stronger ARI itself with higher aerosol

527 concentrations in Pattern 5 and the more apparent CRI inhibition with denser cloud liquid water
528 contents under the LT pattern (Fig. 5). Therefore, the intensity of CRI inhibition of ARI in the
529 SCB was altered by synoptic forcing, with stronger effects under the influence of LT.

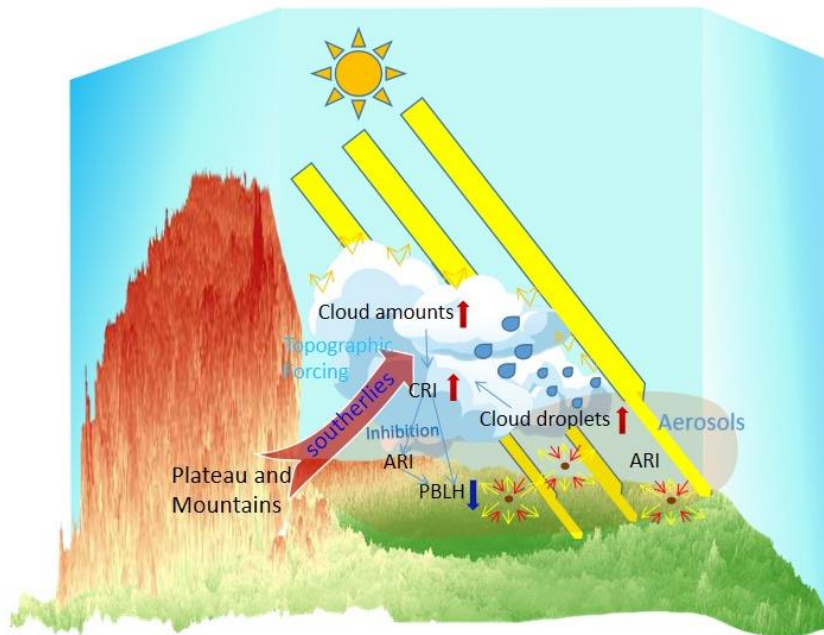


Figure 12. The aerosol radiative effect can be significantly inhibited by cloud under influence of pollution synoptic patterns with dense cloud.

530

531 **4 Conclusion**

532 This study utilized synoptic classification and numerical simulation to gain insights into the
533 combined effects of synoptic patterns and CRI inhibition on ARI and PBL structures in the wet and
534 cloudy SCB. Based on the long-term $PM_{2.5}$ observations and sounding data in the SCB, it was
535 found that large-scale synoptic circulations at 850 hPa played crucial roles in the variations of
536 $PM_{2.5}$ pollution. Synoptic classification was performed with the T-PCA method, which revealed
537 that Pattern 2 and 5 characterized with low pressure system and southerly airflow on 850 hPa were
538 key synoptic patterns for onset and accumulation of $PM_{2.5}$, while Pattern 1 controlled by the
539 northerly airflow represented a clean pattern associated with significant decrease in $PM_{2.5}$.
540 Moreover, it was indicated that Pattern 2 and 5 exhibited denser cloud liquid water content and
541 thus stronger compared to other patterns. Among these patterns, Pattern 5 exhibited the highest
542 cloud liquid water content and CRI. This could be attributed to the robust southerly airflow
543 induced by the dense isobaric lines, which brought warm and humid air masses into the region.

544 To illustrate the interactions among cloud, aerosol and PBL under pollution synoptic patterns, a
545 pollution episode occurred from January 1 to 7, 2017, was simulated with using WRF-Chem. The

546 simulation results showed that ARI remarkably reduced solar radiation was during the two
547 pollution patterns. This reduction led to surface cooling in the morning and upper-air warming in
548 the afternoon. Additionally, the enhanced evening surface cooling was impacted by the mountain-
549 valley wind circulations forced by the plateau-basin topography of the SCB. This modulation in
550 the vertical thermal structure by the ARI would then suppress the development of the PBL,
551 favoring pollution outbreaks (Fig. 12). Furthermore, parallel simulation experiments indicated that
552 CRI impacted stratification stability and modulated the vertical thermal structure by inhibiting ARI
553 (Fig. 12). Regarding the spatial distribution, a stronger ARI appeared in Chongqing, despite lower
554 PM_{2.5} concentrations compared to the western and southern SCB. This was due to the lower cloud
555 liquid water content and weaker CRI inhibition of ARI in Chongqing. When CRI inhibition was
556 not considered, the ARI in the western and southern SCB was significantly stronger than that in
557 Chongqing. In addition, under Pattern 5, the reduction in solar radiation and PBLH during the
558 daytime due to ARI could be more than doubled when the CRI influence was neglected. This was
559 primarily due to higher aerosol concentrations and cloud liquid water contents associated with a
560 low trough in Pattern 5. This study provided insights into the interaction among aerosols, clouds,
561 and PBL under different synoptic patterns, considering the complex terrain and foggy/cloudy
562 climate of the SCB. The findings highlighted the significant role of CRI inhibition on ARI during
563 wet and cloudy conditions, shedding light in the multi-scale atmospheric physical processes in the
564 SCB.

565 **Author contributions.** HL and MX had the original idea for the study, designed the experiments,
566 conducted the numerical simulation and prepared the initial draft manuscript. BL, YZ and KZ
567 collected the data. TW and BZ helped perform the analysis with constructive discussions, reviewed and
568 edited the manuscript. HL, MX, TW and BL acquired financial support for the project leading to this
569 publication. SL and ML reviewed the manuscript.

570 **Competing Interest:** The authors declare no conflict of interest.

571 **Data Available Statement**

572 The ERA5 pressure layer and single layer data can be respectively downloaded from
573 <https://cds.climate.copernicus.eu/cdsapp#!/dataset/reanalysis-era5-pressure-levels> and
574 <https://cds.climate.copernicus.eu/cdsapp#!/dataset/reanalysis-era5-single-levels?tab=form>.
575 The NCEP FNL data are available at <https://rda.ucar.edu/datasets/ds083.2/>. The MEIC data can
576 be accessed in Zheng et al (2018) at <https://doi.org/10.5194/acp-18-14095-2018>. Air quality and
577 meteorological monitoring data can be acquired from <https://doi.org/10.7910/DVN/USX59E>.

578 **Financial support:** This work was supported by the National Natural Science Foundation of China
579 (42205186, 42275102), the Chongqing Natural Science Foundation (cstc2021jcyj-msxmX1007),
580 Special Science and Technology Innovation Program for Carbon Peak and Carbon Neutralization of
581 Jiangsu Province (BE2022612), the key technology research and development of Chongqing

582 Meteorological Bureau (YWJSGG-202215; YWJSGG-202303) and the research start-up fund for the
583 talented person recruitment of Nanjing Normal University (184080H201B57).

584 **References**

- 585 Alexeeff, S., Deosaransingh, K., Liao, N., Van Den Eeden, S., Schwartz, J., and Sidney, S. (2021) Particulate
586 Matter and Cardiovascular Risk in Adults with Chronic Obstructive Pulmonary Disease, *American*
587 *journal of respiratory and critical care medicine* 204(2): 159-167.
- 588 Cao, S., Zhang, S., Gao, C., Yan, Y., Bao, J., Su, L., Liu, M., Peng, N., and Liu, M. (2021) A long-term analysis of
589 atmospheric black carbon MERRA-2 concentration over China during 1980–2019, *Atmospheric*
590 *Environment* 264, 118662.
- 591 Chen, Z., Chen, D., Zhao, C., Kwan, M.-p., Cai, J., Zhuang, Y., Zhao, B., Wang, X., Chen, B., Yang, J., Li, R., He,
592 B., Gao, B., Wang, K., and Xu, B. (2020) Influence of meteorological conditions on PM_{2.5}
593 concentrations across China: A review of methodology and mechanism, *Environment International* 139,
594 105558.
- 595 Ding, A., Huang, X., Nie, W., Sun, J., Kerminen, V.-M., Petäjä, T., Su, H., Cheng, Y., Yang, X.-Q., Wang, M.,
596 Chi, X., Wang, J. P., Virkkula, A., Guo, W., Yuan, J., Wang, S., Zhang, R. J., Wu, Y., Song, Y., and Fu,
597 C. (2016) Black carbon enhances haze pollution in megacities in China, *Geophysical Research Letters*
598 43(6):2873-2879.
- 599 ECMWF (2017). Part IV: Physical processes, In IFS documentation CY43R3 (pp. 1–221). England: European
600 Centre for Medium-Range Weather Forecasts. Retrieved from <https://www.ecmwf.int/node/17736>.
- 601 Eresmaa, N., Karppinen, A., Joffre, S. M., Räsänen, J., & Talvitie, H. (2006). Mixing height determination by
602 ceilometer. *Atmos. Chem. Phys.*, 6(6), 1485-1493. <https://doi.org/10.5194/acp-6-1485-2006>.
- 603 Fast, J. D., Gustafson, W. I., Easter, R. C., Zaveri, R. A., Barnard, J. C., Chapman, E. G., Grell, G. A., and
604 Peckham, S. E.: Evolution of ozone, particulates, and aerosol direct radiative forcing in the vicinity of
605 Houston using a fully coupled meteorology-chemistry-aerosol model, *J. Geophys. Res.-Atmos.*, 111,
606 D21305, <https://doi.org/10.1029/2005jd006721>, 2006.
- 607 Feng, X., Wei, S., and Wang, S. (2020) Temperature inversions in the atmospheric boundary layer and lower
608 troposphere over the Sichuan Basin, China: Climatology and impacts on air pollution, *Science of The*
609 *Total Environment* 726, 138579.
- 610 Garratt, J. R. (1994) Review: the atmospheric boundary layer, *Earth-Science Reviews* 37, 89-134.
- 611 Gong S, Liu Y, He J, Zhang L, Lu S, Zhang X. (2022) Multi-scale analysis of the impacts of meteorology and
612 emissions on PM_{2.5} and O₃ trends at various regions in China from 2013 to 2020 1: Synoptic circulation
613 patterns and pollution. *Sci Total Environ.* Apr 1;815:152770.
- 614 Grell, G. A., Peckham, S. E., Schmitz, R., McKeen, S. A., Frost, G., Skamarock, W. C., and Eder, B. (2005) Fully
615 coupled “online” chemistry within the WRF model, *Atmospheric Environment* 39, 6957-6975.
- 616 Grell, G. A., & Freitas, S. R. (2013). A scale and aerosol aware convective parameterization. *Atmos. Chem. Phys.*
617 14(10), 5233–5250.
- 618 Guenther, A., Karl, T., Harley, P., Wiedinmyer, C., Palmer, P. I., and Geron, C. (2006) Estimates of global
619 terrestrial isoprene emissions using MEGAN (Model of Emissions of Gases and Aerosols from Nature),
620 *Atmos. Chem. Phys.* 6, 3181-3210.
- 621 Guo, J., Miao, Y., Zhang, Y., Liu, H., Li, Z., Zhang, W., ... & Zhai, P. (2016) The climatology of planetary
622 boundary layer height in China derived from radiosonde and reanalysis data. *Atmospheric Chemistry and*
623 *Physics*, 16(20), 13309-13319.
- 624 Hansen, J., Sato, M., and Ruedy, R. (1997) Radiative forcing and climate response, 102, 6831-6864.

625 Haywood, J. M., Abel, S. J., Barrett, P. A., Bellouin, N., Blyth, A., Bower, K. N., Brooks, M., Carslaw, K., Che,
626 H., Coe, H., Cotterell, M. I., Crawford, I., Cui, Z., Davies, N., Dingley, B., Field, P., Formenti, P.,
627 Gordon, H., de Graaf, M., Herbert, R., Johnson, B., Jones, A. C., Langridge, J. M., Malavelle, F.,
628 Partridge, D. G., Peers, F., Redemann, J., Stier, P., Szpek, K., Taylor, J. W., Watson-Parris, D., Wood, R.,
629 Wu, H., and Zuidema, P. (2021) The CLOUD–Aerosol–Radiation Interaction and Forcing: Year 2017
630 (CLARIFY-2017) measurement campaign, *Atmos. Chem. Phys.* 21, 1049-1084.

631 Hong, S.-Y., Dudhia, J., and Chen, S.-H. (2004) A Revised Approach to Ice Microphysical Processes for the Bulk
632 Parameterization of Clouds and Precipitation, *Monthly Weather Review* 132, 103-120.

633 Hong, S. Y., Y. Noh, and J. Dudhia (2006), A new vertical diffusion package with an explicit treatment of
634 entrainment processes, *Mon. Weather Rev.*, 134(9), 2318-2341.

635 Hu, J., Zhao, T., Liu, J., Cao, L., Xia, J., Wang, C., Zhao, X., Gao, Z., Shu, Z., and Li, Y. (2021) Nocturnal surface
636 radiation cooling modulated by cloud cover change reinforces PM_{2.5} accumulation: Observational study
637 of heavy air pollution in the Sichuan Basin, Southwest China, *Science of The Total Environment* 794,
638 148624.

639 Huth, R. (1996) AN INTERCOMPARISON OF COMPUTER-ASSISTED CIRCULATION CLASSIFICATION
640 METHODS, *International Journal of Climatology* 16, 893-922.

641 Huth, R., Beck, C., Philipp, A., Demuzere, M., Ustrnul, Z., Cahynová, M., Kyselý, J., and Tveito, O. E. (2008)
642 Classifications of Atmospheric Circulation Patterns, *Ann N Y Acad Sci*, 1146, 105-152.

643 Iacono, M. J., Delamere, J. S., Mlawer, E. J., Shephard, M. W., Clough, S. A., and Collins, W. D. (2008),
644 Radiative forcing by long-lived greenhouse gases: Calculations with the AER radiative transfer models, *J.*
645 *Geophys. Res.*, 113, D13103.

646 Jiang, Y., Xin, J., Zhao, D., Jia, D., Tang, G., Quan, J., Wang, M., & Dai, L. (2021). Analysis of differences
647 between thermodynamic and material boundary layer structure: Comparison of detection by ceilometer
648 and microwave radiometer. *Atmospheric Research*, 248, 105179.
649 <https://doi.org/https://doi.org/10.1016/j.atmosres.2020.105179>.

650 Jiménez, P. A., & Dudhia, J. (2012). Improving the Representation of Resolved and Unresolved Topographic
651 Effects on Surface Wind in the WRF Model. *Journal of Applied Meteorology and Climatology*, 51(2),
652 300-316. <https://doi.org/https://doi.org/10.1175/JAMC-D-11-084.1>.

653 Li, K., Liao, H., Mao, Y., and Ridley, D. A. (2016) Source sector and region contributions to concentration and
654 direct radiative forcing of black carbon in China, *Atmospheric Environment* 124, 351-366.

655 Li, J., Wu, M., Li, Y., Ma, S., Wang, Z., Zhao, Y., et al. (2021a). Reinforcement of secondary circulation by
656 aerosol feedback and PM_{2.5} vertical exchange in the atmospheric boundary layer. *Geophysical Research*
657 *Letters*, 48, e2021GL094465.

658 Li, Q., Wu, B., Liu, J., Zhang, H., Cai, X., and Song, Y. (2020) Characteristics of the atmospheric boundary layer
659 and its relation with PM_{2.5} during haze episodes in winter in the North China Plain, *Atmospheric*
660 *Environment* 223, 117265.

661 Li, X., Miao, Y., Ma, Y., Wang, Y., and Zhang, Y. (2021b) Impacts of synoptic forcing and topography on aerosol
662 pollution during winter in Shenyang, Northeast China, *Atmospheric Research* 262, 105764.

663 Li, Z., Wang, Y., Guo, J., Cribb, M., Dong, X., Fan, J., Gong, D.-Y., Huang, J., Jiang, M., Jiang, Y., Lee, S. S., Li,
664 H., Li, J., Liu, J., Qian, Y., Rosenfeld, D., Shan, S., Sun, Y., Wang, H., and Zheng, Y. (2019) East Asian
665 Study of Tropospheric Aerosols and their Impact on Regional Clouds, Precipitation, and Climate
666 (EAST-AIR CPC), *Journal of Geophysical Research: Atmospheres* 124(23):13026-13054.

667 Liao, Z., Jielan, X., Fang, X., Wang, Y., Zhang, Y., Xu, X., and Fan, S. (2020) Modulation of synoptic circulation
668 to dry season PM_{2.5} pollution over the Pearl River Delta region: An investigation based on self-
669 organizing maps, *Atmospheric Environment* 230, 117482.

670 Liu, N., Zhou, S., Liu, C., and Guo, J. (2019) Synoptic circulation pattern and boundary layer structure associated
671 with PM_{2.5} during wintertime haze pollution episodes in Shanghai, *Atmospheric Research* 228, 186-195.

672 Lohmann, U., and Feichter, J. (2005) Global indirect aerosol effects: a review, *Atmos. Chem. Phys.* 5, 715-737.

673 Lu H, Xie M, Liu B, Liu X, Feng J, Yang F, Zhao X, You T, Wu Z, Gao Y. (2022) Impact of atmospheric
674 thermodynamic structures and aerosol radiation feedback on winter regional persistent heavy particulate
675 pollution in the Sichuan-Chongqing region, China. *Sci Total Environ.* Oct 10;842:156575.

676 Lu, H., Xie, M., Liu, X., Liu, B., Jiang, M., Gao, Y., & Zhao, X. (2021). Adjusting prediction of ozone
677 concentration based on CMAQ model and machine learning methods in Sichuan-Chongqing region,
678 China. *Atmospheric Pollution Research*, 12(6), 101066.
679 <https://doi.org/https://doi.org/10.1016/j.apr.2021.101066>.

680 Ma, S., Shao, M., Zhang, Y., Dai, Q., and Xie, M. (2021) Sensitivity of PM_{2.5} and O₃ pollution episodes to
681 meteorological factors over the North China Plain, *Science of The Total Environment* 792, 148474.

682 Miao, Y., Che, H., Zhang, X., and Liu, S. (2020) Integrated impacts of synoptic forcing and aerosol radiative effect
683 on boundary layer and pollution in the Beijing–Tianjin–Hebei region, China, *Atmos. Chem. Phys.* 20,
684 5899-5909.

685 Miao, Y., Che, H., Zhang, X., and Liu, S. (2021) Relationship between summertime concurring PM_{2.5} and O₃
686 pollution and boundary layer height differs between Beijing and Shanghai, China, *Environmental
687 Pollution* 268, 115775.

688 Miao, Y., Guo, J., Liu, S., Liu, H., Li, Z., Zhang, W., and Zhai, P. (2017) Classification of summertime synoptic
689 patterns in Beijing and their associations with boundary layer structure affecting aerosol pollution,
690 *Atmospheric Chemistry and Physics* 17, 3097-3110.

691 Nandan, R., Madineni, V. R., Kiran, R., & Naik, D. (2021). Retrieval of cloud liquid water path using radiosonde
692 measurements: Comparison with MODIS and ERA5. *Journal of Atmospheric and Solar-Terrestrial
693 Physics*, 227, 105799. <https://doi.org/10.1016/j.jastp.2021.105799>.

694 Ning, G., Wang, S., Ma, M., Ni, C., Shang, Z., Wang, J., and Li, J. (2017) Characteristics of air pollution in
695 different zones of Sichuan Basin, China, *The Science of the total environment* 612, 975-984.

696 Ning, G., Yim, S. H. L., Wang, S., Duan, B., Nie, C., Yang, X., Wang, J., and Shang, K. (2019) Synergistic effects
697 of synoptic weather patterns and topography on air quality: a case of the Sichuan Basin of China,
698 *Climate Dynamics* 53, 6729-6744.

699 Ojo, J. S., Ayeni, D., & Ogunjo, S. T. (2023). Comparative analysis between ERA5 reanalysis data and MRR
700 observation data at different altitudes for fall velocity and liquid water content. *Advances in Space
701 Research*, 72(6), 2217-2225. <https://doi.org/https://doi.org/10.1016/j.asr.2023.05.045>.

702 Painemal, D., Chellappan, S., Smith, W. L. Jr., Spangenberg, D., Park, J. M., Ackerman, A., et al. (2023).
703 Wintertime synoptic patterns of midlatitude boundary layer clouds over the western North Atlantic:
704 Climatology and insights from in situ ACTIVATE observations. *Journal of Geophysical Research:
705 Atmospheres*, 128, e2022JD037725. <https://doi.org/10.1029/2022JD037725>.

706 Peng, J., Hu, M., Shang, D., Wu, Z., Du, Z., Tan, T., Wang, Y., Zhang, F., & Zhang, R. (2021). Explosive
707 Secondary Aerosol Formation during Severe Haze in the North China Plain. *Environmental Science &
708 Technology*, 55(4), 2189-2207. <https://doi.org/10.1021/acs.est.0c07204>.

709 Pilinis, C., Seinfeld, J. H., and Grosjean, D. (1989) Water content of atmospheric aerosols, *Atmospheric
710 Environment* 23, 1601-1606.

711 Pöschl, U., Martin, S. T., Sinha, B., Chen, Q., Gunthe, S. S., Huffman, J. A., Borrmann, S., Farmer, D. K., Garland,
712 R. M., Helas, G., Jimenez, J. L., King, S. M., Manzi, A., Mikhailov, E., Pauliquevis, T., Petters, M. D.,
713 Prenni, A. J., Roldin, P., Rose, D., Schneider, J., Su, H., Zorn, S. R., Artaxo, P., and Andreae, M. O.

714 (2010) Rainforest Aerosols as Biogenic Nuclei of Clouds and Precipitation in the Amazon, 329, 1513-
715 1516.

716 Qi, N.; Tan, X.; Wu, T.; Tang, Q.; Ning, F.; Jiang, D.; Xu, T.; Wu, H.; Ren, L. (2022) Deng, W. Temporal and
717 Spatial Distribution Analysis of Atmospheric Pollutants in Chengdu–Chongqing Twin-City Economic
718 Circle. *Int. J. Environ. Res. Public Health*, 19, 4333. <https://doi.org/10.3390/ijerph19074333>.

719 Rosenfeld, D., Lohmann, U., Raga, G. B., O'Dowd, C. D., Kulmala, M., Fuzzi, S., Reissell, A., and Andreae, M. O.
720 (2008) Flood or Drought: How Do Aerosols Affect Precipitation?, *Science* 321, 1309-1313.

721 Seibert, P., Beyrich, F., Gryning, S.-E., Joffre, S., Rasmussen, A., & Tercier, P. (2000). Review and
722 intercomparison of operational methods for the determination of the mixing height. *Atmospheric*
723 *Environment*, 34(7), 1001-1027. [https://doi.org/https://doi.org/10.1016/S1352-2310\(99\)00349-0](https://doi.org/https://doi.org/10.1016/S1352-2310(99)00349-0).

724 Schell, B., Ackermann, I. J., Hass, H., Binkowski, F. S., and Ebel, A. (2001) Modeling the formation of secondary
725 organic aerosol within a comprehensive air quality model system, *Journal of Geophysical Research:*
726 *Atmospheres* 106, 28275-28293.

727 Scott Archer-Nicholls, Douglas Lowe, David M. Schultz, and Gordon McFiggans. (2016) Aerosol–radiation–cloud
728 interactions in a regional coupled model: the effects of convective parameterisation and resolution,
729 *Atmos. Chem. Phys.*, 16, 5573–5594.

730 Shu, Z., Liu, Y., Zhao, T., Xia, J., Wang, C., Cao, L., Wang, H., Zhang, L., Zheng, Y., Shen, L., Luo, L., and Li, Y.
731 (2021) Elevated 3D structures of PM_{2.5} and impact of complex terrain-forcing circulations on heavy haze
732 pollution over Sichuan Basin, China, *Atmos. Chem. Phys.* 21, 9253-9268.

733 Skamarock, W. C., Klemp, J. B., Dudhia, J., Gill, D. O., Barker, D., Duda, M. G., ... Powers, J. G. (2008). A
734 Description of the Advanced Research WRF Version 3 (No. NCAR/TN-475+STR). University
735 Corporation for Atmospheric Research. doi:10.5065/D68S4MVH.

736 Stockwell, W. R., Middleton, P., Chang, J. S., and Tang, X. (1990) The second generation regional acid deposition
737 model chemical mechanism for regional air quality modeling, *Journal of Geophysical Research:*
738 *Atmospheres* 95, 16343-16367.

739 Su, T., Li, Z., and Kahn, R. (2018) Relationships between the planetary boundary layer height and surface
740 pollutants derived from lidar observations over China: regional pattern and influencing factors, *Atmos.*
741 *Chem. Phys.* 18, 15921-15935.

742 Tewari, M., Chen, F., Wang, W., Dudhia, J., Lemone, M. A., ... Mitchell, K. E. (2004). Implementation and
743 verification of the unified Noah land-surface model in the WRF model [presentation]. In 20th
744 Conference on Weather Analysis and Forecasting/16th Conference on Numerical Weather Prediction.
745 American Meteorological Society: Seattle, WA, US.

746 Twomey, S. (1977) The Influence of Pollution on the Shortwave Albedo of Clouds, *Journal of Atmospheric*
747 *Sciences* 34, 1149-1152.

748 Wang, C., Jia, M., Xia, H., Wu, Y., Wei, T., Shang, X., Yang, C., Xue, X., and Dou, X. (2019) Relationship
749 analysis of PM_{2.5} and boundary layer height using an aerosol and turbulence detection lidar, *Atmos.*
750 *Meas. Tech.* 12, 3303-3315.

751 Wang, D., Jensen, M. P., Taylor, D., Kowalski, G., Hogan, M., Wittmann, B. M., Rakotoarivony, A., Giangrande,
752 S. E., and Park, J. M. (2022) Linking Synoptic Patterns to Cloud Properties and Local Circulations Over
753 Southeastern Texas, *Journal of Geophysical Research: Atmospheres* 127, e2021JD035920.

754 Wang, P., Qiao, X., & Zhang, H. (2020). Modeling PM_{2.5} and O₃ with aerosol feedbacks using WRF/Chem over
755 the Sichuan Basin, southwestern China. *Chemosphere*, 254, 126735.
756 <https://doi.org/https://doi.org/10.1016/j.chemosphere.2020.126735>.

757 Wang, Z., Huang, X., and Ding, A. (2018) Dome effect of black carbon and its key influencing factors: a one-
758 dimensional modelling study, *Atmos. Chem. Phys.* 18, 2821-2834.

759 Wang, Y., Gao, W., Wang, S., Song, T., Gong, Z., Ji, D., Wang, L., Liu, Z., Tang, G., Huo, Y., Tian, S., Li, J., Li,
760 M., Yang, Y., Chu, B., Petäjä, T., Kerminen, V.-M., He, H., Hao, J., Kulmala, M., Wang, Y., and Zhang,
761 Y. (2020) Contrasting trends of PM_{2.5} and surface-ozone concentrations in China from 2013 to 2017,
762 National Science Review 7, 1331-1339.

763 Wu, Z., Xie, M., Gao, Y., Lu, H., Zhao, L., Gao, S., (2018). Inversion of SO₂ emissions over chongqing with
764 ensemble square root kalman filter. Research of Environmental Sciences 31, 25–33.

765 Xiao, Q., Zheng, Y., Geng, G., Chen, C., Huang, X., Che, H., Zhang, X., He, K., and Zhang, Q. (2021) Separating
766 emission and meteorological contributions to long-term PM_{2.5} trends over eastern China during 2000–
767 2018, Atmos. Chem. Phys. 21, 9475-9496.

768 Xie, M., Liao, J., Wang, T., Zhu, K., Zhuang, B., Han, Y., Li, M., and Li, S. (2016) Modeling of the anthropogenic
769 heat flux and its effect on regional meteorology and air quality over the Yangtze River Delta region,
770 China, Atmospheric Chemistry and Physics 16, 6071-6089.

771 Xie, M., Zhu, K., Wang, T., Feng, W., Gao, D., Li, M., Li, S., Zhuang, B., Han, Y., Chen, P., and Liao, J. (2016)
772 Changes in regional meteorology induced by anthropogenic heat and their impacts on air quality in
773 South China, Atmos. Chem. Phys. 16, 15011-15031.

774 Xu, Y., Xue, W., Lei, Y., Huang, Q., Zhao, Y., Cheng, S., Ren, Z., and Wang, J. (2020) Spatiotemporal variation
775 in the impact of meteorological conditions on PM_{2.5} pollution in China from 2000 to 2017, Atmospheric
776 Environment 223, 117215.

777 Yang, T., Chen, R., Gu, X., Xu, J., Yang, L., Zhao, J., Zhang, X., Bai, C., Kang, J., Ran, P., Shen, H., Wen, F.,
778 Huang, K., Chen, Y., Sun, T., Shan, G., Lin, Y., Wu, S., Zhu, J., Wang, R., Shi, Z., Xu, Y., Ye, X., Song,
779 Y., Wang, Q., Zhou, Y., Ding, L., Yang, T., Yao, W., Guo, Y., Xiao, F., Lu, Y., Peng, X., Zhang, B.,
780 Xiao, D., Wang, Z., Zhang, H., Bu, X., Zhang, X., An, L., Zhang, S., Cao, Z., Zhan, Q., Yang, Y., Liang,
781 L., Cao, B., Dai, H., van Donkelaar, A., Martin, R. V., Wu, T., He, J., Kan, H., and Wang, C. (2021)
782 Association of fine particulate matter air pollution and its constituents with lung function: The China
783 Pulmonary Health study, Environment International 156, 106707.

784 Yang Dasheng, Wang Pucai. 2012. Characteristics of Vertical Distributions of Cloud Water Contents over China
785 during Summer. Chinese Journal of Atmospheric Sciences, 36(1): 89-101.

786 Yao, B., Liu, C., Yin, Y., Liu, Z., Shi, C., Iwabuchi, H., & Weng, F. (2020). Evaluation of cloud properties from
787 reanalyses over East Asia with a radiance-based approach. Atmos. Meas. Tech., 13(3), 1033-1049.
788 <https://doi.org/10.5194/amt-13-1033-2020>.

789 Yin, Z., and Wang, H. (2017) Role of atmospheric circulations in haze pollution in December 2016, Atmos. Chem.
790 Phys. 17, 11673-11681.

791 Yu, R., Wang, B., and Zhou, T. (2004) Climate Effects of the Deep Continental Stratus Clouds Generated by the
792 Tibetan Plateau, Journal of Climate 17, 2702-2713.

793 Zhan, C.-c., Xie, M., Fang, D.-x., Wang, T., Wu, Z., Lu, H., Li, M.-m., Chen, P., Zhuang, B.-l., Li, S., Zhang, Z.-q.,
794 Gao, D., Reng, J.-y., and Zhao, M. (2019) Synoptic weather patterns and their impacts on regional
795 particle pollution in the city cluster of the Sichuan Basin, China, Atmospheric Environment 208(1): 34-
796 47.

797 Zhan, C., Xie, M., Lu, H., Liu, B., Wu, Z., Wang, T., Zhuang, B., Li, M., and Li, S. (2023) Impacts of urbanization
798 on air quality and the related health risks in a city with complex terrain, Atmos. Chem. Phys., 23, 771–
799 788,

800 Zhang, J., Lin, Z., 1985. Climate in China. Shanghai Publication House, Shanghai, p. 603.

801 Zhang, S., Zeng, G., Wang, T., Yang, X., and Iyakaremye, V. (2022) Three dominant synoptic atmospheric
802 circulation patterns influencing severe winter haze in eastern China, Atmos. Chem. Phys. 22, 16017-
803 16030.

804 Zhang, Y., Ding, A., Mao, H., Nie, W., Zhou, D., Liu, L., Huang, X., and Fu, C. (2015) Impact of synoptic weather
805 patterns and inter-decadal climate variability on air quality in the North China Plain during 1980–2013,
806 *Atmospheric Environment* 124, Part B: 119-128.

807 Zhao, B., Liou, K.-N., Gu, Y., Li, Q., Jiang, J. H., Su, H., He, C., Tseng, H.-L. R., Wang, S., Liu, R., Qi, L., Lee,
808 W.-L., and Hao, J. (2017) Enhanced PM_{2.5} pollution in China due to aerosol-cloud interactions,
809 *Scientific Reports* 7, 4453.

810 Zhao, C., Yang, Y., Fan, H., Huang, J., Fu, Y., Zhang, X., Kang, S., Cong, Z., Letu, H., and Menenti, M. (2020)
811 *Aerosol characteristics and impacts on weather and climate over the Tibetan Plateau*, *National Science*
812 *Review* 7, 492-495.

813 Zhao, S., Yu, Y., Yin, D., Qin, D., He, J., and Dong, L. (2017) Spatial patterns and temporal variations of six
814 criteria air pollutants during 2015 to 2017 in the city clusters of Sichuan Basin, China, *The Science of*
815 *the total environment* 624, 540-557.

816 Zheng, B., Tong, D., Li, M., et al. (2018) Trends in China's anthropogenic emissions since 2010 as the
817 consequence of clean air actions, *Atmos. Chem. Phys.*, 18, 14095-14111.

818 Zhong, J., Zhang, X., Wang, Y., Wang, J., Shen, X., Zhang, H., Wang, T., Xie, Z., Liu, C., Zhang, H., Zhao, T.,
819 Sun, J., Fan, S., Gao, Z., Li, Y., and Wang, L. (2019) The two-way feedback mechanism between
820 unfavorable meteorological conditions and cumulative aerosol pollution in various haze regions of China,
821 *Atmospheric Chemistry and Physics* 19, 3287-3306.

822 Zhong, J., Zhang, X., Yunsheng, D., Wang, Y., Liu, C., Wang, J., Zhang, Y., and Che, H. (2018) Feedback effects
823 of boundary-layer meteorological factors on cumulative explosive growth of PM_{2.5} during winter heavy
824 pollution episodes in Beijing from 2013 to 2016, *Atmospheric Chemistry and Physics* 18, 247-258.

825 Zhou, M., Zhang, L., Chen, D., Gu, Y., Fu, T.-M., Gao, M., Zhao, Y., Lu, X., and Zhao, B. (2019) The impact of
826 aerosol–radiation interactions on the effectiveness of emission control measures, *Environmental*
827 *Research Letters* 14, 024002.